Mon. Not. R. Astron. Soc. **000**, 1–26 (2011) Printed 11 July 2012 (MN LATEX style file v2.2)

The XMM-Newton serendipitous ultraviolet source survey catalogue

M.J. Page[1], C. Brindle[1], A. Talavera[2], M. Still[1,3], S.R. Rosen[1,4], V.N. Yershov[1], H. Ziaeepour[1,5], K.O. Mason[1,6], M.S. Cropper[1], A.A. Breeveld[1], N. Loiseau[2], R. Mignani[1,7], A. Smith[1], P. Murdin[8]

[1] *Mullard Space Science Laboratory, University College London, Holmbury St Mary, Dorking, Surrey, RH5 6NT, UK*
[2] *XMM-Newton Science Operations Centre, ESA, Villafranca del Castillo, Apartado 78, 28691 Villanueva de la Cañada, Spain*
[3] *NASA Ames Research Center, Moffett Field, CA 94035, USA*
[4] *Department of Physics and Astronomy, University of Leicester, Leicester LE1 7RH, UK*
[5] *Max Planck Institut für Extraterrestrische Physik (MPE), Giessenbachstrasse 1, 85748 Garching, Germany*
[6] *Science and Technology Facilicities Council, Polaris House, North Star Avenue, Swindon, Wilts SN2 1SZ, UK*
[7] *Kepler Institute of Astronomy, University of Zielona Góra, Lubuska 2, 65-265 Zielona Góra, Poland*
[8] *Institute of Astronomy, Madingley Road, Cambridge CB3 0HA, UK*

Accepted —-. Received —-; in original form —-

ABSTRACT

The *XMM-Newton* Serendipitous Ultraviolet Source Survey (XMM-SUSS) is a catalogue of ultraviolet (UV) sources detected serendipitously by the Optical Monitor (XMM-OM) on-board the *XMM-Newton* observatory. The catalogue contains ultraviolet-detected sources collected from 2 417 XMM-OM observations in 1–6 broad band UV and optical filters, made between 24 February 2000 and 29 March 2007. The primary contents of the catalogue are source positions, magnitudes and fluxes in 1 to 6 passbands, and these are accompanied by profile diagnostics and variability statistics. The XMM-SUSS is populated by 753 578 UV source detections above a 3σ signal-to-noise threshold limit which relate to 624 049 unique objects. Taking account of substantial overlaps between observations, the net sky area covered is 29–54 deg^2, depending on UV filter. The magnitude distributions peak at $m_{\rm AB} = 20.2$, 20.9 and 21.2 in UVW2 ($\lambda_{eff} = 2120$Å), UVM2 ($\lambda_{eff} = 2310$Å) and UVW1 ($\lambda_{eff} = 2910$Å) respectively. More than 10 per cent of sources have been visited more than once using the same filter during *XMM-Newton* operation, and > 20 per cent of sources are observed more than once per filter during an individual visit. Consequently, the scope for science based on temporal source variability on timescales of hours to years is broad. By comparison with other astrophysical catalogues we test the accuracy of the source measurements and define the nature of the serendipitous UV XMM-OM source sample. The distributions of source colours in the UV and optical filters are shown together with the expected loci of stars and galaxies, and indicate that sources which are detected in multiple UV bands are predominantly star-forming galaxies and stars of type G or earlier.

Key words: astrometry – catalogues – galaxies: photometry – stars: general – ultraviolet: general.

1 INTRODUCTION

One of the instruments carried by the European Space Agency's *XMM-Newton* satellite is the Optical Monitor, an ultraviolet/optical telescope with a 30cm diameter primary mirror (Mason et al., 2001). While its main rationale is to provide complementary data to those from the X-ray instruments, and in particular to create a simultaneous multi-wavelength capability to constrain spectral energy distributions, *XMM-Newton* Optical Monitor (XMM-OM) is a capable instrument in its own right. With a field of 17x17 arcmin^2 and a full width half maximum of the point spread function of less than 2 arcsec over the full field of view, XMM-OM provides a powerful UV survey capability over much larger fields than is possible with the *Hubble Space Telescope* UV

instrumentation, and at a finer spatial sampling than provided by the *GALEX* satellite (Martin et al., 2005).

A UV survey capability for XMM-OM was envisaged at the inception of the instrument concept in 1988, and the UV filter choice and observation strategies were planned to maximise the UV survey science return. At that time, in addition to sounding rocket observations, UV photometric surveys had been carried out by the *Orbiting Astronomical Observatory 2* (Code et al., 1970; Davis et al., 1972), *TD-1* (Boksenberg et al., 1973; de Jager et al., 1974) and the *Astronomical Netherlands Satellite* (van Duinen et al., 1975). They were augmented by other surveys including from *Skylab* (Henize et al., 1975), *Apollo 16* (Carruthers, 1973) and *Apollo 17* (Henry et al., 1975). These had provided first generation views of the UV sky. While the *IUE* satellite launched in 1978 (Boggess et al., 1978) carried out more than 10^5 UV spectroscopic observations over a period of 17 years, the imaging, and therefore large-scale knowledge of the UV sky remained surprisingly limited.

During the 1990s, a broader but still limited view of the UV sky was achieved using imagers on the Space Shuttle (FAUST, Bowyer *et al.,* 1993, UIT, Stecher *et al.,* 1997), and then much more detailed views using *HST*, initially with the Faint Object Camera (Albrecht & Jakobsen, 2002), followed by the Wide Field and Planetary Camera 2 (Trauger et al., 1994), the Space Telescope Imaging Spectrograph (Kimble et al., 1998), the Advanced Camera for Surveys (Sirianni et al., 2005) and the Wide Field Camera 3 (MacKenty et al., 2010).

XMM-Newton with XMM-OM was launched in 1999, followed in 2003 by *GALEX* (Martin et al., 2005) and in 2005 by *Swift* with its Ultraviolet and Optical Telescope (Roming et al., 2005, UVOT), of a similar design to XMM-OM. The imaging passbands of XMM-OM and *GALEX* are given in Table 1; the UVOT on *Swift* has similar passbands to XMM-OM. The era of large-scale UV surveys to faint limiting magnitudes had arrived. *GALEX* in particular has sampled nearly the full sky, outside of the Galactic plane, through two broadband filters covering the near-UV and far-UV respectively.

This paper describes the *XMM-Newton* Serendipitous Ultraviolet Source Survey (XMM-SUSS), an electronic catalogue of UV sources detected serendipitously by the XMM-OM. The catalogue contains ultraviolet source detections collected from 2 417 *XMM-Newton* observations made between 24 February 2000 and 29 March 2007. Taking account of substantial overlaps between observations, the net sky area covered ranges from 29 to 54 deg^2 depending on UV filter. The primary content of the catalogue is source positions and photometry in up to 3 UV filters and 3 optical filters for 624 049 unique UV sources. This is accompanied by spatial extent and variability diagnostics.

With respect to the *GALEX* All-sky Imaging Survey (AIS) and Medium Imaging Survey (MIS), the XMM-SUSS covers a much smaller sky area, reaching magnitudes intermediate between the AIS and MIS, but has finer photometric sampling in wavelength, better morphological discrimination, and less susceptibility to source confusion. The latter point, which is a consequence of the XMM-OM having a much finer instrumental point spread function than *GALEX* (FWHM $\leqslant$ 2 arcsec compared to 4–5 arcsec; see Table 1), is particularly important for the fidelity of the XMM-SUSS in crowded regions such as the Galactic plane and Magellanic Clouds. The XMM-SUSS also has the advantage that the UV observations were obtained simulaneously with sensitive X-ray imaging, the source content of which is easily accessible through the 2XMM catalogue (Watson et al., 2009). Furthermore, many of the XMM-SUSS sources were observed more than once per filter during an *XMM-Newton* observation and/or through multiple *XMM-Newton* visits. Consequently, the scope for science based on temporal source variability on timescales of hours to years is broad.

XMM-SUSS is a release originating from the XMM-OM instrument team on behalf of ESA and coordinated with the *XMM-Newton* Science Survey Centre (SSC, Watson et al., 2001). An alternative, independent catalogue of XMM-OM sources (OMCat), based on an earlier version of the *XMM-Newton* Science Analysis Software (SAS), is described in Kuntz et al. (2008). Since 2008, the XMM-SUSS has been available from the *XMM-Newton* Science Archive[1], NASA HEASARC[2], the XMM-SUSS project pages[3] and through the VO interfaces. An initial announcement of the catalogue was made in Still et al. (2008).

This paper is laid out as follows. The instrumentation and data selection are described in Section 2 and the data processing is described in Section 3. In Section 4 we describe the tests which were carried out to check the quality and reliability of the catalogue. The properties of the catalogue are described in Section 5. A brief description of the differences between the XMM-SUSS and the OMCat is provided in Section 6. Known issues wih the XMM-SUSS, and our plans for future development are described in Section 7. Our conclusions are presented in Section 8. Testing and validation of the source detection algorithm used for XMM-SUSS are given in Appendix A. Details of the quality flagging algorithms are given in Appendix B and a list and description of the columns in the XMM-SUSS source table are given in Appendix C.

2 INSTRUMENTATION AND DATA SAMPLE

2.1 The XMM-Newton Optical Monitor

The XMM-OM is a 30-cm optical/UV telescope of a modified Ritchey Chrétien design, coaligned with the X-ray telescopes (Mason et al., 2001). From the primary mirror, incoming light is reflected via the secondary mirror onto a rotatable, flat mirror which directs the beam onto one of two identical filter wheel and detector assemblies.

Each of the XMM-OM detectors consists of a photon-counting micro-channel plate (MCP) intensified Charge Coupled Device (CCD) (Fordham et al., 1989). Incident photons eject electrons from a multi-alkali (S20) photo-cathode, optimized to UV and blue wavelengths, which are amplified by a factor 10^6 in number using MCPs in series. These electrons strike a phosphor screen, the photons from which are fed to the CCD via a fibre-optic taper. By centroiding the photon cascade on the CCD, the sky positions of incident photons are determined by on-board software to a

[1] http://xmm.esac.esa.int/xsa/
[2] http://heasarc.gsfc.nasa.gov
[3] http://www.mssl.ucl.ac.uk/www_astro/XMM-OM-SUSS

degree of precision which is much higher than the physical CCD pixel size. An image is constructed in real time onboard which subsamples the CCD array by factor 8, providing data of 2048 × 2048 pixels of size 0.476 × 0.476 arcsec^2. The onboard centroiding gives rise to a low-level modulo-8 fixed-pattern distortion (Kawakami et al., 1994) which is routinely corrected in the ground processing. The detector response is linear when the arrival rate of events per photon-cascade resolution element[4] is significantly below the CCD readout frame rate, typically 90–140 s^{-1}. At higher count rates, the detector response is non-linear, an effect known as coincidence-loss (Fordham, Moorhead & Galbraith, 2000). This effect becomes significant ($\sim$ 10 per cent) at around 0.1 counts per frame (typically corresponding to sources of 2.3 – 2.8 magnitudes brighter than the zeropoints listed in Table 1). It is corrected for during ground processing, but as sources approach saturation (approximately 5.5 – 6 magnitudes brighter than the zeropoints listed in Table 1) the photometric measurement errors become larger, rather than smaller, with count rate (Kuin & Rosen, 2008). At very high count rates, centroiding of multiple, overlapping photon splashes in each frame causes the point spread function to become distorted, and bright sources are surrounded by regions of coincidence-loss-induced modulo-8 noise which cannot be corrected in ground processing.

The detector design results in zero readout noise and a low level of dark noise. Above the Earth's atmosphere the small aperture of the XMM-OM is compensated by its UV sensitivity and the absence of atmospheric extinction and diffraction. Sky background is dominated by diffuse zodiacal and Galactic light. XMM-OM is therefore well-suited to detecting faint sources. CCD pixel-to-pixel sensitivity variations are unimportant, cosmetic CCD defects cause few image defects, and large scale sensitivity gradients are small. Cosmic rays are discriminated and eliminated on board.

Both the position and arrival time of photons are recorded on-board. Non-dispersive observations can be performed in two modes, IMAGING mode (with no recorded photon arrival times) and FAST mode, which time-tags each photon. IMAGING mode provides the largest field-of-view available at the expense of timing information. The largest image available is 17×17 arcmin^2, although commonly smaller windows are used to either tailor an observation to specific science goals or to meet telemetry or onboard storage limits. The allowed exposure times of IMAGING mode exposures range from 800 s to 5000 s. FAST mode can be achieved within the onboard memory budget only if the window is small, typically 10.5 × 10.5 arcsec^2. IMAGING mode data are typically obtained in parallel during FAST mode observing. The majority of IMAGING data are binned 2 × 2 onboard to 1″ × 1″ image pixels. In most cases the full field of view is sampled during an observation in at least one filter, either using a full-frame IMAGING mode or by mosaicing smaller IMAGING windows obtained in series. Modes are discusseed more fully in Mason et al. (2001) and Ehle et al. (2008).

XMM-Newton's 48h orbit allows for long, uninterrupted pointings of science targets. The XMM-OM typically takes

[4] the group of physical CCD pixels containing a photon splash, as distinct from the image resolution

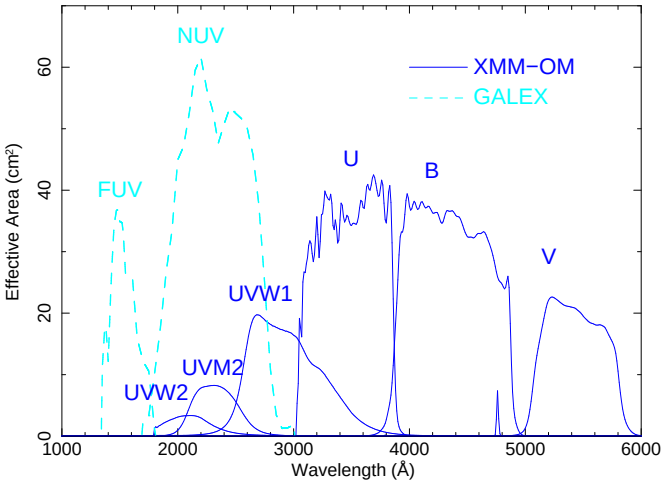

Figure 1. Effective areas of the XMM-OM pass bands (solid-lines) together with those of *GALEX* (dashed-lines). The small peak at 4760Å is part of the U filter response. The sharp cutoff in the UVW2 pass band is due to the materials used in the optical elements rather than the filter itself.

multiple exposures of the same field through several filters, sometimes with a sequence of differing IMAGING mode windows in order to cover the full field of view. Individual sources are often recorded more than once through the same filter where either sub-windows overlap or exposures are repeated.

There are seven imaging filters mounted in the XMM-OM filter wheel together with two grisms for low-dispersion spectroscopy. One of the filters, WHITE, transmits over the full XMM-OM bandpass (1800–8000Å) to maximise throughput. The remaining filters in the order of increasing central wavelength are called UVW2, UVM2, UVW1, U, B and V, where the final three filters cover similar wavelength ranges to the Johnson UBV set (Johnson & Morgan, 1951). The effective areas of the XMM-OM imaging passbands are shown in Fig. 1 together with those of *GALEX*. Although not visible in Fig. 1, the response curves of the UVW2 and UVM2 filters extend beyond 3000Å into the optical range, and the UVW1 response curve extends beyond 4100Å, albeit with very low throughput (< 0.1 cm^2). The basic properties of the XMM-OM passbands are listed in Table 1.

2.2 Data selection

The XMM-SUSS is derived from 2 417 *XMM-Newton* observations obtained between 24 February 2000 and 29 March 2007, all of which are publicly available in the *XMM-Newton* science archive. Because the XMM-SUSS is a catalogue of UV sources, only those *XMM-Newton* observations which include at least one XMM-OM exposure through the UVW2, UVM2 or UVW1 filters were considered for the catalogue.

The catalogue is constructed entirely from data taken in IMAGING mode. FAST mode data are excluded because of the small window size. Similarly, 2 × 2 arcmin^2 unbinned central windows of the default imaging configuration are ignored, although note that in the majority of observations, the central region is also recorded as an 8 × 8 arcmin^2 image which is included within the catalogue sample. Data taken with the WHITE filter provide very limited colour informa-

Table 1. Characteristics of the XMM-OM imaging passbands. The corresponding numbers for the *GALEX* FUV and NUV passbands are given for comparison; *Swift UVOT* has similar passbands to XMM-OM. The wavelength ranges are for an effective area > 10 per cent of peak. Note that U filter has a small additional region of sensitivity around 4760Å in addition to the wavelength range given below (see Fig. 1). Fluxes in the XMM-SUSS correspond to the effective wavelengths listed. The corresponding numbers for *GALEX* are taken from Morrissey et al. (2007).

	XMM-OM						*GALEX*	
	UVW2	UVM2	UVW1	U	B	V	FUV	NUV
Effective Wavelength (Å)	2120	2310	2910	3440	4500	5430	1539	2316
Wavelength range (Å)	1800–2550	1990–2700	2430–3610	3030–3890	3810–4900	5020-5870	1344–1786	1771–2831
Zero point (AB)	16.57	17.41	18.57	19.19	19.08	17.92	18.82	20.08
Peak effective area (cm^2)	3	8	20	42	39	23	37	62
FWHM resolution (arcsec)	1.98	1.80	2.00	1.55	1.39	1.35	4.2	5.3

tion and so are not utilised for the catalogue. Grism data are not used for the catalogue because of the different nature of the dispersed data and to avoid the source confusion within the grism fields.

The pointing of *XMM-Newton* is usually good to 3 arcsec. Boresight positions of each field are corrected by comparison of XMM-OM sources with the USNO-B1.0 catalogue, although a minimum number of source detections are required to perform the correction accurately. Images were not used for the catalogue if they contain < 5 source detections, if the RMS residual between matched source positions and their USNO-B counterparts is > 1.5 arcsec, or if the 1σ error in the computed boresight correction is > 1.0 arcsec in either the right ascension or declination directions.

Both the source detection algorithm and aperture photometry become increasingly uncertain in crowded fields owing to source confusion and the lack of background measures. Images were excluded from the catalogue if they had a detected source density > 35 $arcmin^{-2}$, corresponding to 10 000 sources within a full-frame image. The majority of fields excluded by this criterion are U, B and V observations of the Galactic plane and Magellanic Clouds.

Finally, mosaiced images for each field were inspected visually for obvious problems. Images which were dominated by large scattered light features from bright, off-axis sources, those with evidence of telemetry corruption, and those which showed signs of spurious attitude drift were excluded from the catalogue. The distribution of exposure times of the images which were used for the XMM-SUSS, by bandpass, are shown in Fig. 2.

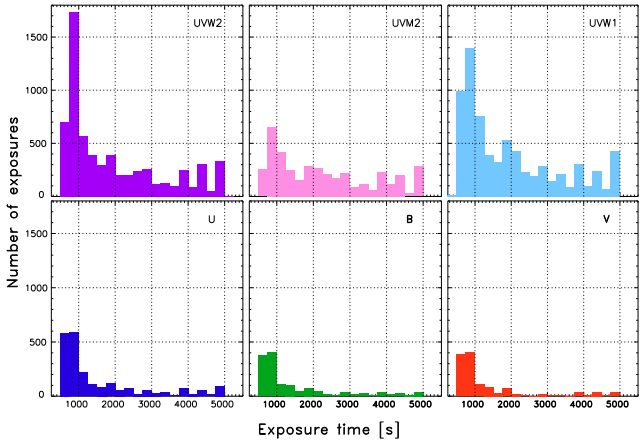

Figure 2. Exposure times of the XMM-OM images used to construct the XMM-SUSS, split by filter.

3 DATA PROCESSING

The data were processed using software tasks from the *XMM-Newton* SAS version 8.0. A number of improvements to the SAS, in particular to the source detection task OMDETECT, were driven by the development of the XMM-SUSS and are implemented in the public release of the SAS (versions 8.0 and higher) so that source lists of comparable quality to the XMM-SUSS are generated by the standard *XMM-Newton* pipeline and distributed as pipeline products, or can be produced by members of the scientific community as required. Of the procedures described in this section, only the merging and concatenation of the source lists for the catalogue (Section 3.10) is carried out outside the standard suite of SAS tasks.

3.1 Raw data

A description of the raw XMM-OM data delivered by the *XMM-Newton* spacecraft is available in Guainazzi & Santos-Lleó (2004). Spacecraft pointing history from independent on-board star trackers is telemetered down with the XMM-OM data. The XMM-OM also records tracking history data from its own dedicated tracking mode windows.

Data required to convert the brightness, position and extent of detected XMM-OM sources from detector units to physical units have been calibrated by the XMM-OM Instrument Team and are stored in the *XMM-Newton* Current Calibration File, which is accessible from the *XMM-Newton* Science Operations Centre web pages[5]. The current state of the XMM-OM calibration is given by Talavera (2011). All raw data employed to construct the XMM-SUSS catalog are in the public domain and can be downloaded from the *XMM-Newton* Science Archive.

3.2 Bad pixels

No attempt is made to correct or interpolate over damaged or contaminated detector pixels. Positions of pixels which do not image the sky (at the corners of the array) and detector defects (Fig. 3) are instead recorded within the Current

[5] http://xmm.esac.esa.int/

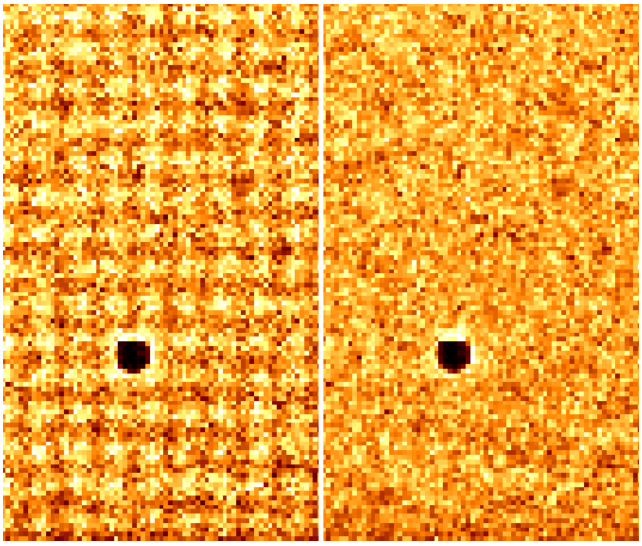

Figure 3. The two images above contain the same exposure taken of a featureless laboratory calibration source. The image on the left was the one delivered by the instrument where the uniform background allows us to easily identify the modulo-8 pixel fixed-pattern structure. The image on the right is the same data after the fixed-pattern has been corrected. The dark area of the image is a dead CCD pixel.

Calibration File. Bad pixels are masked from photometric measures, and sources including bad pixels are flagged as having additional unquantified uncertainties associated with their brightness and location. It is left to the catalog user's discretion whether to include or exclude such sources from their data samples.

3.3 Bias, dark-current and spatial response variations

Owing to the photon-counting nature of the detector, there is no CCD bias level to subtract from images. The dark count rate is below 5×10^{-4} counts s^{-1} pix^{-1} and varies across the detector by < 10 per cent. Therefore dark counts make only a small contribution to the background compared to the zodiacal light, and no attempt is made to separate these two background components within the data processing. Source and background extraction regions are small and from the same image locale, and hence the variation of the dark current over the detector is not a significant factor for source extraction. To within measurement uncertainties, the sensitivity is uniform (to within 5 per cent) with spatial position over the detector, and hence no correction is applied for spatial sensitivity variations.

3.4 Fixed-pattern image structure

As described in Section 2.1 the onboard event centroiding leads to a modulo-8 fixed pattern structure on the raw images, with a peak to peak amplitude of typically 10–20 per cent (see Fig. 3). It should be noted that because the pattern originates from the centroiding process, it is a distortion in the positioning of counts only, and is therefore flux-conserving. The pattern repeats on a 4 arcsec scale (the CCD pixel size), so it is larger than the point source FWHM, but smaller than the generic 5.7 arcsec radius point source and 7.5–12.2 arcsec background apertures used to generate catalog photometry (see Section 3.6). The amplitude and precise structure of the mod-8 pattern vary slowly over the detector.

Dividing out the mod-8 pattern or Fourier-filtering to remove it would not conserve flux and would therefore bias the catalogue photometry. The approach is therefore to measure the amplitude and form of the structure within a cell of dimensions 16×16 CCD pixels (or 64×64 arcsec^2), which slides over the image in order to account for variations due to detector position and local count rates. At each step, the mean background value is calculated with pixels containing sources and cosmetic defects discarded using an iterative clipping algorithm if they deviate from the mean by $\pm6\sigma$. The assumption is made that the remaining fixed pattern does not vary across the cell before the pixels are resized individually so that the background is rendered statistically uniform. After the sliding cell has passed over the full image, the image is resampled so that pixel sizes are once again uniform. The process has the effect of redistributing a small fraction of photons between neighbouring pixels in order to reverse the residual errors in the on-board centroiding and minimise the fixed-pattern, while retaining photometric accuracy.

Image backgrounds must be bright enough to provide meaningful statistics within the sliding cell, otherwise the fixed-pattern correction becomes Poisson noise-dominated. In such cases the background level is too low for the fixed-pattern distortion to have any significant impact on the detection or measurement of sources. Therefore if a cell contains <1 000 counts, corresponding to a sensitivity limit of 25 per cent peak-to-peak pattern structure, the correction is not performed. This situation occurs most frequently in short UV exposures.

3.5 Source detection

Source detection is performed in raw detector coordinates in order to simplify the quality flagging. Quality issues such as readout streaks, diffraction spikes and smoke rings (see Section 3.9.3) are most easily diagnosed and kept track of in detector coordinates before rotating, undistorting and translating the image to sky coordinates. The measured detector coordinates of each source are transformed to sky coordinates in a subsequent process.

There are a large number of astronomical software packages for performing source detection on optical images, and most either locate sources by searching for local maxima, or by a thresholding process (see Drory, 2003). The former method is usually the most efficient way to detect point sources, whilst the latter one is more suited for extended sources. Because of the large range in OM image background values encountered (from <1 count per pixel in the UV to >400 counts per pixel in the optical) and issues specific to the OM images (e.g. scattered-light features, modulo-8 patterns around bright sources), OM images are reduced using the SAS task OMDETECT, which uses both peak-finding and thresholding algorithms in order to detect both point and extended sources as efficiently and reliably as possible. Details of the testing and validation of the OMDETECT source

detection algorithm are given in Appendix A. A brief outline of how it works follows.

OMDETECT first constructs a background map and a noise map which are used to set the detection threshold. The background level at a particular pixel location is computed using the median value of the pixel values in a box 50 arcsec on a side, centred at that position, ignoring pixels which were above a certain height above a global median and using a simple clipping algorithm. Each pixel of the noise map is computed using the standard deviation of the pixel values used at that particular point in the background map.

The sources on an image are detected in a number of stages. The first stage uses a peak finding algorithm to find mainly point-like sources. A list of all the pixels above a background threshold is obtained, and, in order of decreasing pixel value, each one is checked to see if it could be part of a point source. In checking the pixels in this order, point sources are generally detected in order of decreasing brightness and the detection of faint spurious sources in the wings of bright sources is largely overcome. A validation function is used which checks the profile shapes of sources for consistency with the point-spread function and image binning. If a source passes the validation tests, the pixels associated with it are identified and used to compute the position, FWHM of the major axis, FWHM of the minor axis and position angle using intensity-weighted moments (for more details see Section 4.4). The source is then classified as either point-like or extended from a comparison of the FWHM of the major axis with the FWHM of the point-spread function. If the FWHM of the major axis is larger than the FWHM of the point spread function by more than 3 times the major-axis FWHM uncertainty, the source is classified as extended; otherwise it is classified as point-like. The detection process is repeated a number of times using different validation functions and thresholds to find as many point sources as possible. Each validation function is fine-tuned to identify a particular kind of point source (e.g. very bright sources surrounded by a modulo-8 distortion, sources with one or more close neighbours, sources near an image edge). Few sources at this stage are classified as extended.

The next stage is to locate extended sources, and for this purpose an image segmentation algorithm is used. A map of the pixels above a given height above the background map is obtained and the number of pixels within each cluster is checked to ensure that it lies within specified bounds; those clusters that do not are discarded. The remaining pixel clusters are examined using a validation function. The validation function carries out various checks (e.g. pixel geometry, proximity to bright point sources, axial-ratio) and if the pixel cluster passes the checks its position, FWHM of the major axis, FWHM of the minor axis and position angle are computed using intensity-weighted moments. As in the previous stage, the source is classified as point-like or extended according to whether its major-axis FWHM exceeds the FWHM of the point spread function by more than 3σ. The process is repeated several times to find both large and small extended sources. A special validation function is used to attempt to identify scattered light regions. Some of these features can be identified by their cirrus-like nature, which leads to a distribution of source pixels containing many holes, and by comparing the total number of holes to the total number of cluster pixels a decision is made whether or not the source is a scattered-light feature. If it is a scattered-light feature then these pixels are subsequently ignored.

A final detection stage locates very faint point sources which may have been missed in the point-source detection stage for various reasons (e.g. there being too few pixels to compare the profile with that of the PSF). This uses the extended source detection algorithm with a special validation function for faint sources. The image is first slightly smoothed to help locate faint, extended sources. At the end of the source-detection stage, if any large extended sources have been detected the background map is refined by interpolating across these sources. Each large extended source is then re-examined to see if it can be split into two or more overlapping sources.

After the source-detection passes, all sources are tested for credibility by the following criteria: the centroid of the source must be contained within the cluster of pixels associated with it; the significance of the source (i.e. the ratio of the source counts to the rms background fluctuation in the same aperture) must be > 3 when measured with a 5.7 arcsec (12 unbinned pixel) radius aperture; if the significance in a 5.7 arcsec radius aperture is < 10 the source must also have a significance > 3 in a 2.8 arcsec (6 unbinned pixel) radius aperture. The next stage is to perform photometry on the sources. For each source, the photometry procedure which is applied depends on whether the source was classified as point-like or extended according to whether its major-axis FWHM exceeds the FWHM of the point spread function by more than 3σ.

3.6 Photometry of point sources

Standard, unweighted aperture photometry is performed on each point source. Bad pixels recorded in the quality map (see Section 3.2) are ignored during the pixel summation. The aperture is a circle of radius 5.7 arcsec (12 unbinned pixels), and the background is a 7.5–12.2 arcsec circular annulus. The size of the source aperture is chosen to allow accurate correction for coincidence loss (Section 2.1). The background annulus is adjusted slightly to ensure that the background aperture is 2 full binned-image pixels from the source aperture. If source apertures of neighbouring objects encroach upon either the background or source regions then all contaminated pixels are ignored in the aperture summation.

If the significance of an object is < 10 the source aperture is reduced in size to a 2.8 arcsec radius circle in order to improve the quality of the photometry. For sources with one or more close neighbours the aperture is also reduced in size as necessary to avoid overlapping source apertures, down to a minimum of 2.8 arcsec radius. Reduced-aperture source counts are corrected to their 5.7 arcsec equivalent using a curve-of-growth extrapolation of the calibrated point-spread function (PSF) for the appropriate bandpass, stored in the Current Calibration File.

Before converting source counts to a physical magnitude or flux scale it is necessary to correct for potential photon-coincidence losses (Section 2.1). The brighter a source, the greater the level of coincidence loss. The effect has been calibrated for point sources through observations of photometric standard fields. Coincidence loss distorts the point

spread function at high countrates, so the calibration has been determined for apertures of a fixed size of 5.7 arcsec (12 unbinned pixel) radius, an aperture size which minimises the effect of the distortion on the measured count rate. The coincidence loss correction is therefore applied directly to the counts within these apertures, or for weak sources, to the counts after they have been adjusted to these aperture sizes. For the UVW1, UVM2 and UVW2 filters, the zero-points in the Current Calibration File are for a 16.5 arcsec aperture, and so for these filters a further curve-of-growth correction is now applied to obtain count rates in a 16.5 arcsec aperture.

The XMM-OM has a time-dependent sensitivity variation owing to gradual photocathode degradation. This is calibrated by the XMM-OM instrument team using regular calibration observations and it is recorded in the Current Calibration File. Correction of the source counts for the time-dependent sensitivity variation is performed after the coincidence-loss and aperture corrections. Finally, the source counts are converted to magnitudes and flux densities using the zero points and conversion factors stored in the Current Calibration File. Photometric uncertainties are calculated as Poisson errors, scaled by the same factors (coincidence loss, aperture correction and time-dependent sensitivity) as the source counts. The photometric uncertainties do not include systematic terms related to uncertainties in the coincidence loss or photometric calibration.

3.7 Photometry of extended sources

The aperture for extended source photometry is source-dependent and irregular, containing all pixels associated with the object during the source detection operations. All clustered pixels $> 2\sigma$ above the background are considered to be the same source. Bad pixels recorded in the quality map (Section 3.2) are ignored during the pixel summation. The background level is determined from the background image produced during the source detection process (Section 3.5).

Coincidence losses are calculated for each individual pixel using a 5.7 arcsec aperture centred on the pixel. Both source and background pixels are corrected, and the source counts are obtained by summing all corrected pixels within the source aperture minus the inferred summation of corrected background within the aperture.

The time-dependent sensitivity degradation correction is identical to that applied to point sources. The same zeropoints and flux conversion factors are used for extended sources as for point sources. The magnitudes and fluxes quoted in the catalogue are integrated over the whole aperture, rather than provided per unit area.

3.8 Astrometric correction

The first step in obtaining sky coordinates for sources is to correct their raw detector coordinates for image distortions resulting from the optics and detector (Mason et al., 2001). This distortion correction is stable with time and is stored in the Current Calibration File. After the distortion correction the plate scale is linear, and the source positions on the detector are transformed into sky positions using the pointing information recorded by the *XMM-Newton* star trackers. The *XMM-Newton* attitude control system maintains closely the relative spacecraft pointing once it has settled after a slew between one science field and the next, and in the majority of cases spacecraft drift and jitter are small compared to the XMM-OM PSF. However, the absolute accuracy of the star trackers is a few arcsec, so a fine correction to the aspect solution is performed during pipeline processing. Positions of detected sources are compared to the USNO-B1.0 source catalogue (Monet et al., 2003) and a single linear correction in RA and Dec is converged upon for each image by source matching. No correction is made to the satellite position angle (and hence the rotation of the image) because tests indicate that such a correction is not required. A final aspect refinement is obtained by repeating the source matching after merging the source tables from the individual sub-exposures of an *XMM-Newton* observation. After USNO-registration, the astrometry of individual objects detected in XMM-OM images is limited by systematics in the distortion map, which are currently measured to be 0.7 arcsec rms (Talavera, 2011). A comparison of the XMM-SUSS catalogue positions with positions derived from external catalogues is given in Section 4.1.

Table 2. Source quality flags within the XMM-SUSS catalogue.

Bit	Quality issue
0	Source lies over a bad pixel
1	Source lies on or near a bright readout strip
2	Source lies on or near a smoke ring
3	Source lies on or near a diffraction spike
4	Source is bright with coI-loss-induced mod-8 noise
5	Source lies within the central region of scattered light
6	Source lies close to another bright object
7	Source lies close to or over an image boundary
8	Point source lies over an extended source
9	Point source is too compact

3.9 Quality flagging

Sources which are suspected to originate from an artifact of some kind, or for which the measurements are likely to be compromised in some way, are flagged as such during the construction of the catalogue. Table 2 lists the various quality flags which may be set during the processing. The flags are treated as bits in a binary number, so when they are set, bits 0,1,2,3,4,5,6,7,8,9 are equivalent to the integer numbers 1,2,4,8,16,32,64,128,256 and 512 respectively. For convenience the quality flags are recorded in the catalogue both as integer numbers (the sum of the bit values of the flags which are set) and as strings of true/false logical values. The meaning of these quality flags and criteria by which they are set are described briefly in the following subsections, with some more detailed criteria for flags 1–4 provided in Appendix B. We close this section with a few tips on the use of the flags.

3.9.1 Flag 0: bad pixel

An object is flagged if the photometric aperture used to sum source counts includes any bad pixels, as recorded in the

XMM-OM Current Calibration File, blank areas of image caused by telemetry dropouts, or isolated bright pixels.

3.9.2 Flag 1: readout streak

Readout streaks occur because there is no shutter to block incident photons during the short but finite time the CCD takes to readout. It is a negligible effect in sources with brightness within the useful dynamic range of the instrument, but readout streaks from saturated field sources will both contaminate neighbours situated along the same readout column and cause spurious source detections. The criteria used to identify readout streaks are described in Appendix B. Sources likely to be resulting from, or contaminated by, readout streaks are flagged.

3.9.3 Flag 2: smoke ring

Internal reflection of light within the detector window results in an out of focus ghost image of each source which is displaced radially by the curved detector window. These artifacts are called smoke rings. Smoke rings from sources of brightness bounded within the effective dynamic range of the instrument contain negligible numbers of photons but they are noticeable artifacts in saturated sources. Any sources detected within 19 arcsec from the center of a potential smoke ring could be related to, or have their photometry compromised by, the smoke ring and are flagged as such. It should be noted that there are circumstances in which the source responsible for generating a smoke ring is outside the image in which the smoke ring occurs; such cases will not be flagged.

3.9.4 Flag 3: diffraction spike

The secondary mirror support vanes give rise to diffraction spikes in the brightest sources which provide undesirable image structure around neighbouring sources and generate spurious sources. Sources which are likely to lie close to diffraction spikes are flagged.

3.9.5 Flag 4: bright source surrounded by coincidence-loss-induced modulo-8 pattern

As explained in Section 2.1, sources with countrates approaching 1 count per image-frame are subject to coincidence loss, which distorts the point spread function and gives rise to a modulo-8 pattern in the region surrounding the source. The morphologies of such sources cannot be recovered, and hence they are flagged during the construction of the catalogue. At very high countrates coincidence loss leads to saturation and the photometry of sources cannot be recovered (see Section 2.1). Occasionally, sources approaching saturation can lose counts due to integer wraparound in individual pixels of the raw data. Photometry of sources approaching the saturation limits should always be treated with caution.

3.9.6 Flag 5: central enhanced region

Scattered light from the detector chamfer leads to an annular region of background in the centre of the field of view which is enhanced by more than a factor of 2 with respect to the background over the rest of the field of view. Sources within 1.25 arcmin of the instrument boresight are flagged. Note that the flag indicates that a source is *within the region* corresponding to the central enhancement, whether or not the background level is large enough for the central enhancement to have a significant effect.

3.9.7 Flag 6: close to bright source

The structure around bright sources could lead to spurious sources being detected. Any source within 33 arcsec of a source flagged as bright with coincidence-loss-induced modulo-8 structure (flag 4) is flagged as lying close to a bright source.

3.9.8 Flag 7: image edge

Photometry and astrometry will be compromised if a source is partly outside the imaged area. Sources for which any part of the photometric aperture lies outside the field of view (including the corners of the detector) are flagged.

3.9.9 Flag 8: embedded within extended source (not used)

Photometry of point sources is complicated if they overlap an extended source because both source and background aperture will include some contribution from the extended source. If any pixel of the photometric aperture of a point source is shared by an extended source then the point source is flagged. The flag-8 algorithm did not set this flag for any sources retained in the final, released catalogue, and hence the bit corresponding to flag 8 is, in practice, merely a placeholder.

3.9.10 Flag 9: too compact

Although the XMM-OM SAS processing checks the raw data for image bits which have been corrupted, artifacts are occasionally missed and sources are occasionally found in the reduced images which are too compact to be consistent with the XMM-OM point spread function. Such sources are flagged as they are likely to be spurious.

3.9.11 Advice on using the flags

While we recommend that the user treat any quality-flagged source with caution, we offer here some practical advice on the use of the flags. Flag 0 is in the majority of (though not all) cases benign because OMDETECT uses a relatively large area to compute the moments and photometry. Faint sources, and especially faint, extended sources with flags 1, 2 and/or 5 are potentially spurious, but bright sources (significance > 10) with these flags set are likely to be valid, and their properties robust. The central background enhancement is usually very weak in the UVM2 and UVW2 images, so flag 5 is usually benign in these bandpasses even

for faint sources. The user should be wary of photometry, astrometry and morphology of sources with flag 6 or 7, regardless of source brightness. Photometry of sources with flag 4 set is usually good provided they are not approaching the coincidence-loss limits described in Section 2.1, but morpological information for sources with flag 4 should not be trusted. Sources with flag 9 are potentially spurious, but this flag is rare (only 17 sources in the XMM-SUSS have flag 9 set).

3.10 Merging and concatenation of the sourcelists

A sourcelist is generated for each individual XMM-OM imaging exposure. For each *XMM-Newton* observation, the sourcelists from all the XMM-OM exposures, which may include multiple exposures through the same filter and/or exposures through different filters, are merged to form a single sourcelist for the observation using the SAS task OMSRCLISTCOMB. Objects are identified as being a single unique object if they are displaced by less than 2.0 arcsec, or 3 times the positional uncertainty, whichever is the larger. The resulting source lists have one row per source, and are the building blocks of the catalogue, which is formed from their concatenation. The quantities listed in each source row (position, magnitude, etc) are average quantities from the measurements in individual exposures within the observation. Objects which are identified in multiple *XMM-Newton* observations will have multiple entries in the XMM-SUSS. These objects are allocated the same "SRCNUM" identifier in the catalogue if they are within 2 arcsec (point sources) or 3 arcsec (extended sources) or if they are within 3 times the position uncertainty, of each other. This final stage of concatenating the source lists and matching sources between *XMM-Newton* observations is carried out using software written specifically for the XMM-SUSS, that does not form part of the *XMM-Newton* SAS. Almost all source matches are within 3 arcsec, because only 0.8 per cent of the sources have position uncertainties larger than one arcsec. The minimum 2 or 3 arcsec matching radii are intended to account for systematics in the astrometry such as the slight undersampling of the PSF by the image pixels, and uncertainties in the distortion correction (see Section 3.8). In extended sources, there is the additional issue that morphologies can be different in the different bands, leading to a small (but real) difference in the centroid position.

Choosing a matching radius is a compromise between completeness in matching (which improves as the radius is increased) and minimising the number of spurious matches (which becomes more of a problem as the radius is increased). The matching radii were chosen, and the reliability of the matching process in the OMSRCLISTCOMB task was tested, using a combination of simulations and by visual inspection of the matched sources in real XMM-OM sky images. In the simulations, a master source-list file was created with a given number of sources at a variety of significance levels. Using this master source list a number (up to 1000) of new source lists were generated that had a random fraction of the sources of the master source list, and for which each of the sources is displaced by a random position error. A systematic offset was also introduced in each source list generated to simulate the pointing uncertainty. OMSRCLISTCOMB was then run with these source lists. The merged source list it produced was compared to a cut-down version of the master source list, containing only sources which were used once or more in the generation of source lists with position errors. This testing verified the source matching, and that the algorithm worked well, including in crowded fields.

At the end of the catalogue merging, each unique source is labelled with a unique source number ("SRCNUM") within the catalogue, so that each detection of the same source is labelled with the same SRCNUM.

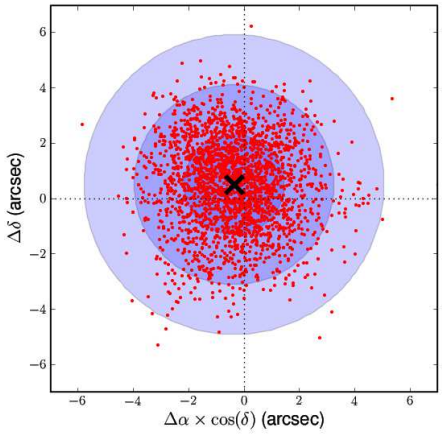

Figure 4. Using source correlations between the XMM-OM source tables and the USNO-B1.0 catalog, systematic corrections are applied to the recorded XMM-OM pointings and source positions. The above plot summarizes the full sample of pointing offsets applied in both the RA (α) and Dec (δ) directions (red dots). The black cross is the mean correction and the blue circles represent 1-, 2- and 3-σ deviations from the mean.

4 VALIDATION OF THE CATALOGUE

In this section we describe the tests which were carried out to check the quality and reliability of the final catalogue.

4.1 Astrometry

The best-fit offsets derived from the astrometric correction process for the XMM-OM images (Section 3.8) are displayed in Fig. 4. The RMS dispersion of the offset distribution is 1.81 arcsec and represents the characteristic absolute accuracy of *XMM-Newton* pointing. The black cross in Fig. 4 represents the mean of the sample and it does not occur at the origin, indicative of a systematic offset in spacecraft pointing, $\langle \Delta\alpha \cos\delta \rangle = -0.36$ arcsec and $\langle \Delta\delta \rangle = +0.50$ arcsec.

The XMM-SUSS source catalogue includes an estimate of the 68 per cent statistical uncertainty in the position of each source. The uncertainties range from 0.05 arcsec to 2.57 arcsec, with a mean position uncertainty of 0.68 arcsec; they do not include any systematic term, although systematics in the distortion correction are known to limit the positional uncertainty to 0.7 arcsec (Talavera, 2011). The histogram in Fig. 5 shows the distribution of angular offsets between individual sources and their nearest USNO matches to a

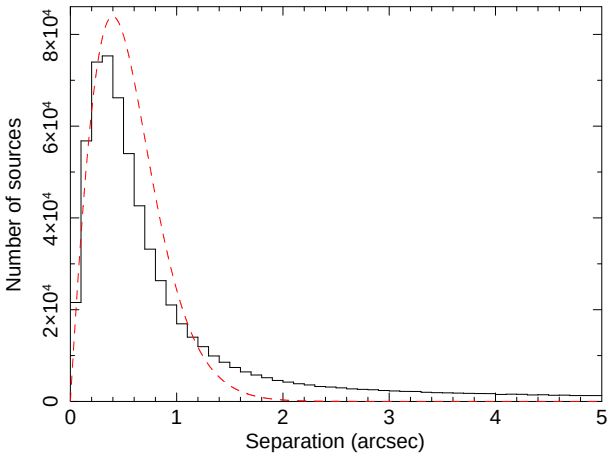

Figure 5. The histogram shows the distribution of angular offsets between all detected sources and their closest matches in the USNO-B1.0 catalogue. The red dashed line is the predicted offset distribution obtained by summing the Rayleigh distributions corresponding to the distribution of position uncertainties.

maximum of 5 arcseconds. If the positional uncertainties in x and y are Gaussian distributed, then we would predict the probability distribution for the offset to be a Rayleigh distribution. The red dashed line in Fig. 5 shows the predicted distribution of offsets, computed as the sum of the Rayleigh distributions corresponding to the sources and their individual positional uncertainties. The real distribution peaks at smaller offsets than the sum of the Rayleigh distributions, but has a tail of associations extending beyond 2 arcseconds. Investigation of sources within this tail shows that 40 per cent have quality flags 6 and/or 7, and so their positional accuracy is degraded because they are close to an image edge, or are affected by the modulo-8 distortion surrounding a bright source. Other likely contributors to the tail include residual systematics related to the distortion map, extended (and asymmetric) sources, for which the offset distribution is inherently non-Rayleigh. The XMM-SUSS sample reaches deeper magnitudes than USNO, so there will also be some contribution to this tail, particularly at the largest offsets, from XMM-SUSS sources which are not detected in USNO and so are spuriously matched to unrelated USNO sources. Overall, 68 per cent of the offsets are within 0.8 arcsec, and 90 percent of the offsets are within 2 arcsec.

As a further check on the XMM-SUSS astrometry, we have cross-checked it against the Guide Star Catalogue version 2.3 (GSC2.3; Lasker et al., 2008), which is independent in the sense that it was not used in the astrometric correction process. We have cross-matched all sources in the XMM-SUSS with the GSC2.3, taking the closest counterpart within a matching radius of 2 arcsec. Note that this cross match compares GSC positions to XMM-SUSS positions *after* the XMM-SUSS astrometry has been corrected using USNO. We found GSC2.3 matches to 314,452 XMM-SUSS sources. We find an average right ascension residual $\langle \Delta\alpha \rangle = 0.06$ arcsec, with a scatter of 0.52 arcsec, while the average declination residual is $\langle \Delta\delta \rangle = 0.03$ arcsec, with a scatter of 0.47 arcsec. The average of the residuals, in both components, is consistent with 0, indicating that there is no significant systematic offset between the astrometry of the XMM-SUSS and the GSC2.3.

4.2 Photometric accuracy

Optical and UV zero-point and colour transformation calibrations are described in Antokhin (2001), Kirsch et al. (2004) and Talavera (2011). These are based upon observations of white dwarf spectrophotometric standards from the International Ultraviolet Explorer (IUE; Fälker et al. 1987) and Space Telescope Imaging Spectrograph (STIS), stored in the CALSPEC database (Bohlin, 2007). While there are no standard UV fields with which to verify independently the accuracy of this calibration, optical photometry can be compared against standard ground-based imaging of photometric standard fields. Fig. 6 compares XMM-OM photometry obtained with the XMM-SUSS pipeline software to the Stetson standards (Stetson, 2000) in the SA95 field (Landolt, 1992) over four mission epochs. Two-colour corrections (Talavera, 2011) have been performed on the OM data to adjust magnitudes to the Johnson B and V bandpasses (Johnson & Morgan, 1951). Objects with quality flags have not been screened from Fig. 6, and are responsible for the obvious outliers.

The XMM-OM and Johnson magnitudes are in good agreement; the median offsets between the XMM-OM and Stetson (2000) photometry for the four epochs combined are 2 and 3 per cent in V and B bands respectively, and the median offsets obtained from the four epochs separately deviate from the overall medians by no more than 2 per cent. The stability of the comparison over the four epochs is testament to the accuracy of time-dependent adjustments made to the calibration in order to compensate for detector degradation.

There is an absence of standard fields for photometric verification of the UV zeropoints. As a rudimentary check on the UV photometry in the XMM-SUSS, we compare the XMM-SUSS sample against the *GALEX* Release 6 (GR6) catalogue (Morrissey et al., 2007). Of the XMM-OM and *GALEX* passbands, the most similar pair is XMM-OM UVM2 and *GALEX* NUV (Fig. 1), though we expect some offset and scatter in photometry betweeen the two bands because the *GALEX* NUV band is much broader than the XMM-OM UVM2. Sources were matched between the XMM-SUSS and *GALEX* samples using a cross-matching distance of 2.0 arcsec. This yields *GALEX* NUV magnitudes for 31 120 XMM-SUSS sources which are detected in UVM2 and have no quality flags. The comparison was restricted to objects for which the photometric uncertainty is less than 0.05 magnitudes in both UVM2 and NUV bands to limit the scatter introduced by photometric errors, reducing the sample to 2 910 objects. The comparison between the *GALEX* and XMM-SUSS photometry is shown in Fig. 7, and shows a strong linear relationship between the two magnitudes over a wide magnitude range. We find a mean magnitude offset of $\langle \mathrm{UVM2}_{AB} - \mathrm{NUV}_{AB} \rangle = -0.026 \pm 0.006$, though with significant scatter in the relation (the standard deviation is 0.33), and the distribution is asymmetric, with a long tail of objects with large $\mathrm{UVM2}_{AB} - \mathrm{NUV}_{AB}$ colours; these are the outliers below the 1:1 line in Fig. 7. Inspection of these outlying objects shows that they are in crowded regions of the sky, sometimes in the outskirts of nearby galaxies, and are blends of multiple sources in the GALEX NUV images. The median $\mathrm{UVM2}_{AB} - \mathrm{NUV}_{AB}$ colour will be robust to these spurious outliers, and is only 0.1. The small offset

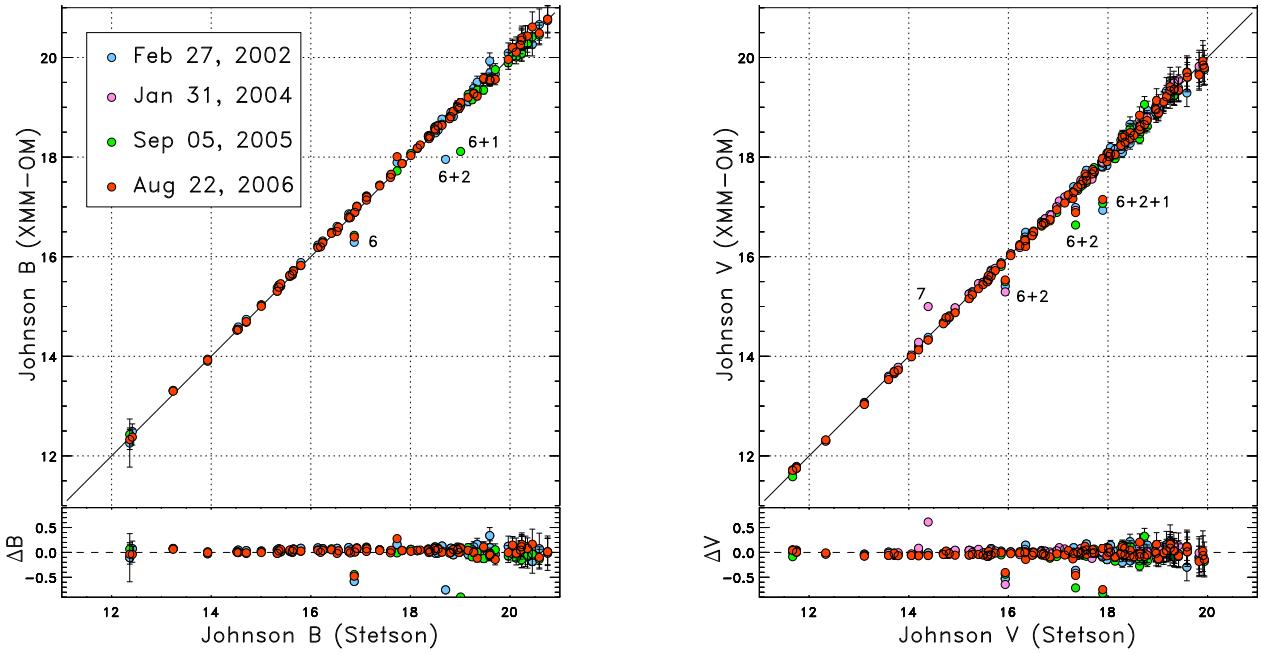

Figure 6. Comparison of XMM-OM and Stetson B and V source magnitudes in the Landolt standard field SA95. XMM-OM magnitudes have been colour-corrected to the Johnson filter system. Lower panels provide the difference between the two measurements. XMM-OM sources were detected over four separate epochs. Photometric outliers have been labelled with the quality flags which apply to them (see Section 3.9 and Table 2).

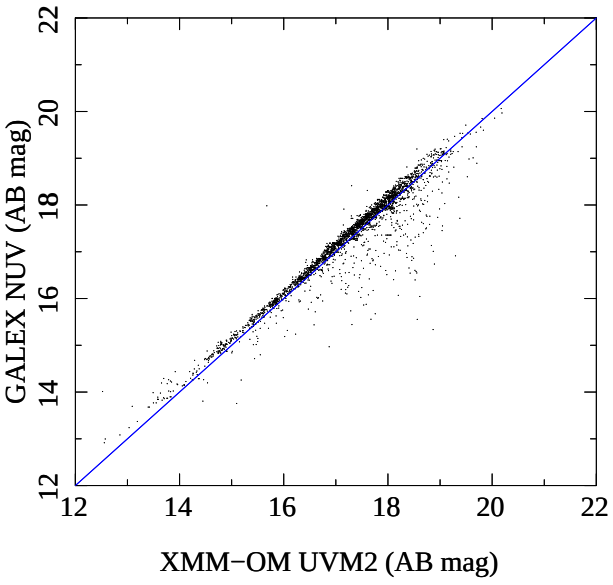

Figure 7. Comparison of XMM-OM UVM2 and *GALEX* NUV magnitudes. A good linear correlation between magnitudes in the two passbands is evident. The blue line corresponds to a 1:1 relation between UVM2 and NUV.

between the median (or mean) UVM2$_{AB}$ and NUV$_{AB}$ magnitudes suggests good consistency between the XMM-SUSS and *GALEX* photometric systems.

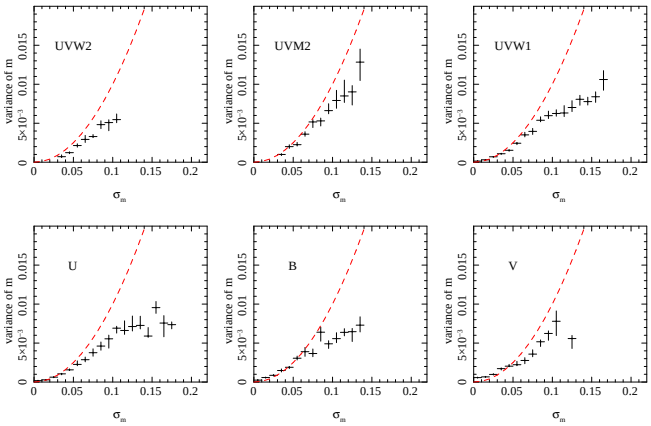

Figure 8. A comparison of the median variance in photometric measurement, for sources observed 4 times or more, as a function of the mean measurement error σ_M, in bins of 0.01 magnitude in σ_M. Errors on the median were obtained by bootstrap resampling of the variance distribution in each bin. The red dashed line shows the expected variance given σ_M.

4.3 Photometric uncertainties

A critical aspect of the catalog data is the statistical error calculated for each photometric measurement. Many fields have been visited more than once by *XMM-Newton*, and repeated measurements of the same sources provide us with a cross-check on the statistical uncertainties given in the catalogue. For each filter, we collate the photometry for each source which has been detected in four or more

XMM-Newton observations with a mean significance of 10 or more, and calculate the variance of the magnitude measurements using the usual equation for sample variance, including Bessel's correction. The significance cut, which is higher than that used for inclusion in the catalogue (see Section 3.5), is included to prevent the detection limit from biasing the variance.[6] For each of these sources, we also calculated the mean of the photometric uncertainties reported in the catalogue for the relevant filter. We then determined the median of the measured variances in 0.01 mag bins of mean photometric uncertainty. Errors on the median were obtained by bootstrap resampling of the variance distributions. The median variances are shown for each filter in Fig. 8. The curve $y = x^2$ represents the expected variance, given the photometric uncertainty reported in the catalogue. Apart from a small excess of variance in the V band (equivalent to 0.02 mag additional photometric scatter), the measured and predicted variances agree well in all filters at small photometric uncertainties ($\sigma_m < 0.05$ mag). This suggests that systematic effects, including large scale sensitivity variations over the face of the detector, currently calibrated to be < 5 per cent (Talavera, 2011), actually contribute no more than a 2 per cent systematic error to the photometric repeatability. For photometric uncertainties $\sigma_m > 0.1$ mag, the median variances lie below the predicted curve, and rise more slowly with σ_m than predicted. This suggests that for $\sigma_m > 0.1$ mag the uncertainties reported in the catalogue are too-conservative (see Section 7). To summarise, the accuracy of the photometry apears to follow the photometric uncertainty σ_m as reported in the catalogue for $\sigma_m < 0.1$ mag, while for $\sigma_m > 0.1$ mag the photometric accuracy appears to be better than reported in the catalogue.

4.4 Extended source parameterisation

The XMM-SUSS catalog provides a measure of source extent and profile on the sky. In these diagnostics, sources are represented crudely as two-dimensional elliptical Gaussian profiles with best-fit orientation of the major axis relative to celestial north. Major and minor axes are characterized by Full-Width Half-Maxima (FWHM), estimated from Gaussian moments. To test the accuracy of the source extent diagnostics, we compare the XMM-OM source profile properties with those associated with optical counterparts within the Sloan Digital Sky Survey (SDSS; York et al., 2000).

A cross-correlation of XMM-SUSS and SDSS DR6 (Adelman-McCarthy et al., 2008) tables, with a positional tolerance of 2 arcsec, yields 65 579 matches. The SDSS catalogue contains flags for source type, based upon empirical properties. 33 143 sources are flagged in SDSS imaging as 'STAR' (i.e. point-like), and 30 629 are flagged as 'GALAXY', i.e. extended sources which are not consistent with the seeing profile of the SDSS image. We segregate point-like sources from extended sources and plot XMM-OM U band magnitude against source extent along the major axis in Fig. 9. While not infallible, the SDSS classification is a good indication of which sources are point-like at the resolution of the XMM-SUSS. Fig. 9 provides confirmation that extended sources are being identified robustly by the SAS pipeline. Neglecting source-mismatches, the overwhelming majority of SDSS point-like sources have XMM-OM detections consistent with a constant FWHM of 2.2 arcsec. Note that the difference between this FWHM and that given in Table 1 is a result of the 2×2 onboard binning undersampling the image. There is an anti-correlation between galaxy extent and magnitude which is a selection effect where diffuse profile wings become increasingly difficult to detect from fainter objects.

The right hand panel of Fig. 9 compares XMM-OM U band extent along the major axis with the corresponding SDSS extent, represented by twice the recorded de Vaucouleurs-law scale radius in the u' band, for sources classified as extended in the SDSS. The XMM-OM U band and SDSS u' bands are chosen for this demonstration because they are the filter bandpasses that most resemble each other. There are two families within this population. There is direct correlation between bright XMM-OM sources and their SDSS counterparts. However compared to the superior depth and angular resolution of the Sloan survey, the XMM-OM is less likely to detect the extended wings of weak (U > 21) sources, resulting in the second population of galaxies, recorded as low-significance, point sources within the XMM-SUSS.

4.5 Visual screening for quality control

To validate the performance of the quality screening, we visually examined 654 exposures which were chosen at random from the observations used for the XMM-SUSS. Sources were noted which have quality issues but had evaded the appropriate quality flag, or which were erroneously flagged. Table 3 gives the fractions of sources flagged with the different quality flags, together with the statistics for missed and erroneous quality flags derived from the visual examination. The statistics provided in Table 3 should be regarded as indicative rather than definitive: only a small fraction of the XMM-SUSS sources have been examined, the visual screening is somewhat subjective, and the importance and incidence of the various quality issues depend quite strongly on filter. Nonetheless, with this caveat it is encouraging to note that in the screened images the maximum fraction of detections, for any quality flag, which was missed by quality flagging, or was erroneously flagged, is 0.2 per cent.

4.6 Matching of sources between wavebands and observations

Source confusion, where two (or more) sources occur close enough together on the sky that they are either blended, or mistakenly identified as the same source, can be an important issue in sky surveys. We estimated the fraction of sources for which the source matching may be complicated or compromised by the close proximity of another source, by searching the XMM-SUSS catalogue for counterparts at sky positions offset in declination by 30 arcsec from the real XMM-SUSS catalogue positions, using the matching radii used to cross-match sources selected in different *XMM-Newton* observations (Section 3.10). This is similar to the

[6] If such a threshold is not applied, the photometric variance for low-significance sources will be artificially reduced, because measurements which are scattered to the fainter magnitudes will be below the detection threshold and so excluded from the catalogue.

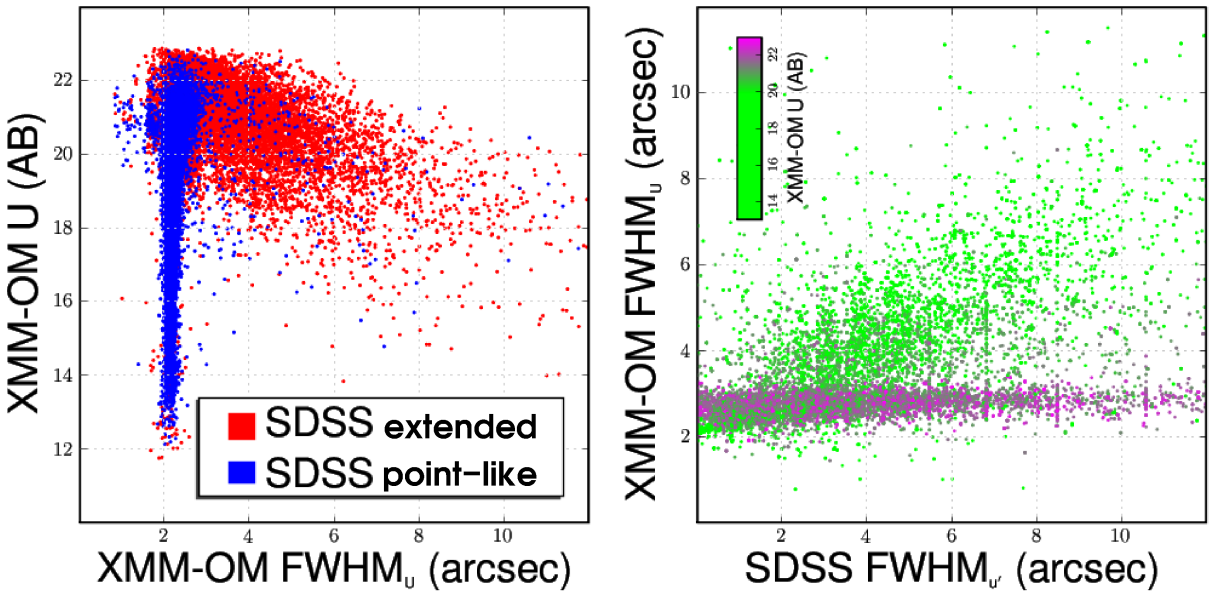

Figure 9. Left panel - XMM-OM U band magnitudes of SDSS DR6 counterparts, plotted against XMM-OM U source extent along the major axis. SDSS sources flagged as point-like and extended are represented by different colours. Right panel - comparison of XMM-OM U band source extent with the counterpart SDSS scale diameter from fits with a de Vaucouleurs model. Colour represents XMM-OM U band magnitude.

Table 3. Overall fractions of detections assigned the different quality flags (Section 3.9). The column labelled 'Detections missed in flagging' gives the fraction of source detections identified in the visual screening which warranted (but lacked) a given flag. The column labelled 'Detections erroneously flagged' gives the fraction of sources which were assigned quality flags which the visual screening indicated were not appropriate. No statistics are given for flag 8 because no sources have been set with this flag in the catalogue.

Flag	Detections flagged (per cent)	Detections missed in flagging (per cent)	Detections erroneously flagged (per cent)
0	1.1	0.001	0.0
1	7.0	0.2	0.06
2	2.6	0.2	0.04
3	0.2	0.2	0.01
4	1.8	0.2	0.06
5	2.3	0.003	0.0
6	1.5	0.2	0.005
7	8.2	0.04	0.0
8	-	-	-
9	0.001	0.0	0.0

method used by Bianchi et al. (2011) to estimate the level of spurious matches between GALEX and SDSS sources. Overall, we find that a counterpart is matched in 2.56 per cent of the random sky positions. We note that a significant fraction of these matches arise in the Galactic plane and Magellanic Clouds fields where the sky density is high. Restricting the estimate to Northern hemisphere fields with $|b| > 20$ deg, the fraction of random sky positions which are matched to a catalogue source drops to 1.0 per cent. From Section 4.1 we see that the majority of offsets between the positions of the same sources in different XMM-OM images will be less than 1 arcsec, while matches to unrelated sources will be distributed uniformly over the source matching area, which is on average 16.5 arcsec^2 in area, so that >80 per cent of the mis-matches will be at distances larger than 1 arcsec. Thus the actual number of mis-matches will be somewhat smaller than the frequency of matches to random sky positions, because the matching algorithm used in the XMM-SUSS takes the most-likely counterpart, which will in the majority of the cases be the correct counterpart. Therefore at high Galactic latitudes and outside the Magellanic Clouds, the likelihood of two different XMM-OM sources being incorrectly associated by the source matching algorithm is less than 0.5 per cent.

In practice, because the point spread function of the XMM-OM is around 2 arcsec FWHM in the UV, source blending in the images is more of a problem than mismatching at the merging stage. Indeed, only 0.05 per cent of the sources have a companion source in the catalogue within 2 arcsec. With so few pairs at small separations there is little scope (or need) to clean the catalogue further by modifying the source-matching algorithm. Where more than one source contributes significantly to the flux in any one band, the source is likely to be flagged as extended in the XMM-SUSS. Selecting only point-sources is therefore likely to exclude the majority of blended sources.

5 CATALOGUE CHARACTERISTICS

In this section we examine the characteristics of the XMM-SUSS that pertain to its scientific use and provide some general properties of the stellar and extragalactic samples.

5.1 Source numbers and sky coverage

There are 753 578 sources within the XMM-SUSS counting multiple detections within an *XMM-Newton* pointing as a single source. Taking into account detections of the same source during different pointings, the number of unique sources within the catalogue is 624 049. Each unique source within the catalogue is assigned a unique identifier (column "SRCNUM"), with which each entry of that source in the catalogue is labelled. Depending on filter, 6–9 per cent of the sources are identified as extended, with the U and B filters having the largest fractions, perhaps because these two passbands have the highest effective areas, and are therefore the most sensitive to faint, extended emission.

The 2 417 XMM-SUSS pointings are shown in Galactic coordinates in Fig. 10. The size of the blue pointing symbols increase in radius and vary in hue as the number of UV sources per pointing increases. Mirroring the wide variety of scientific experiments performed by *XMM-Newton* for its Guest Observers, there are many observations at high Galactic latitude together with clusters of pointings along the Galactic plane, and towards the Magellanic Clouds. Galactic plane and Magellanic Cloud pointings have the largest source densities.

Table 4 lists the total area of sky observed through each filter (taking into account overlapping observations), the fraction of observations which include each filter, and the number of source detections in each band. UVW1, which has the largest throughput of the UV bandpasses, is the default filter for science programs which contain no optical or UV science goals beyond the serendipitous detection of field sources. Consequently, the largest sky area is covered by UVW1, and the largest number of UV source detections (618 266) are made in this band. Indeed, many sources are detected only in UVW1.

The numbers of U, B and V sources are limited in Table 4 by the requirement that only those detected sources with UV counterparts are included within the catalogue. The source content in these filters are also significantly affected by the rejection of fields with $> 10\,000$ source detections in order to avoid crowding and confusion during fine-aspect correction and aperture photometry (Section 2.2). The effective area of XMM-OM peaks in the optical and so UBV data contain a larger fraction of crowded fields compared to the UV sample. As seen in Table 4, B and V observations of the Magellanic Clouds in particular do not make this cut and do not appear within the catalog. One avenue for improving future data releases of the XMM-SUSS will be to improve the fidelity of automated crowded-field data reduction. The fine UV imaging resolution of the XMM-OM is a great asset which will not be fully-exploited in the XMM-SUSS until all UBV counterparts can be incorporated within the catalog accurately.

5.2 Magnitude and signal to noise distributions

Fig. 11 shows the detection significance distribution of all the good-quality sources contained within the catalog, by filter. The step-change in source numbers at 10σ is a consequence of the requirement that sources below this significance level have to pass an additional significance test with a smaller aperture for inclusion in the catalogue (Section 3.5). The different shapes of the UV and optical distributions in Fig. 11 is a result of the requirement that sources must be detected in at least one UV band for inclusion in the catalogue.

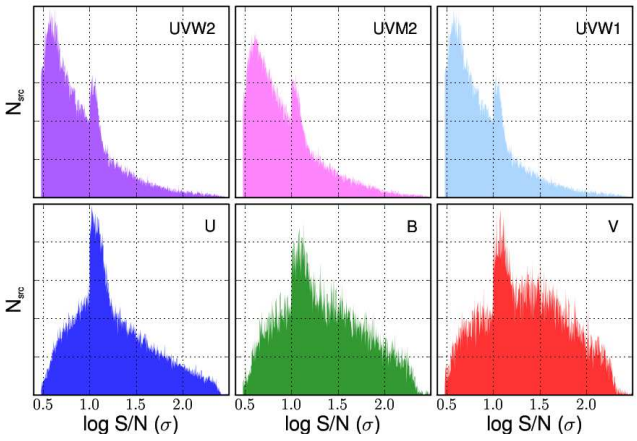

Figure 11. The normalized detection significance distributions of sources with no quality flags contained within the XMM-SUSS catalog, per filter. $N_{\rm src}$ is the number of sources.

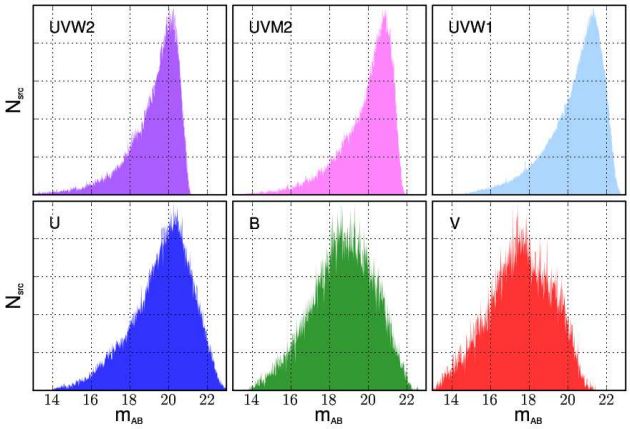

Figure 12. The normalized magnitude distributions of XMM-SUSS sources. Sources with quality flags are not included in the distributions. $m_{\rm AB}$ is the AB magnitude of sources and $N_{\rm src}$ the number of sources contained in each $\Delta m_{\rm AB} = 0.01$ histogram bin.

Fig. 12 shows the filter-dependent magnitude distributions of sources within the XMM-SUSS. Only those sources with no quality flags are included and the distributions are normalized for better comparison. Unlike the sharp, artificial cut-offs displayed by the UV source significance distributions at the low-brightness end (Fig. 11), the UV faint-magnitude distributions cut off more gradually and this is the consequence both of non-uniform exposure lengths and time-variable background levels, resulting in a range of image depth. Magnitude completeness limits thus vary from field to field, but conservative limits at which all fields are essentially complete can be taken as the magnitudes that corresponding to a signal to noise ratio of 10 in an 800s exposure. Using this criterion, we estimate that the survey is complete in all fields down to AB magnitudes of $m_{\rm AB} = 18.1$, 18.8 and 19.4 in UVW2, UVM2 and UVW1 re-

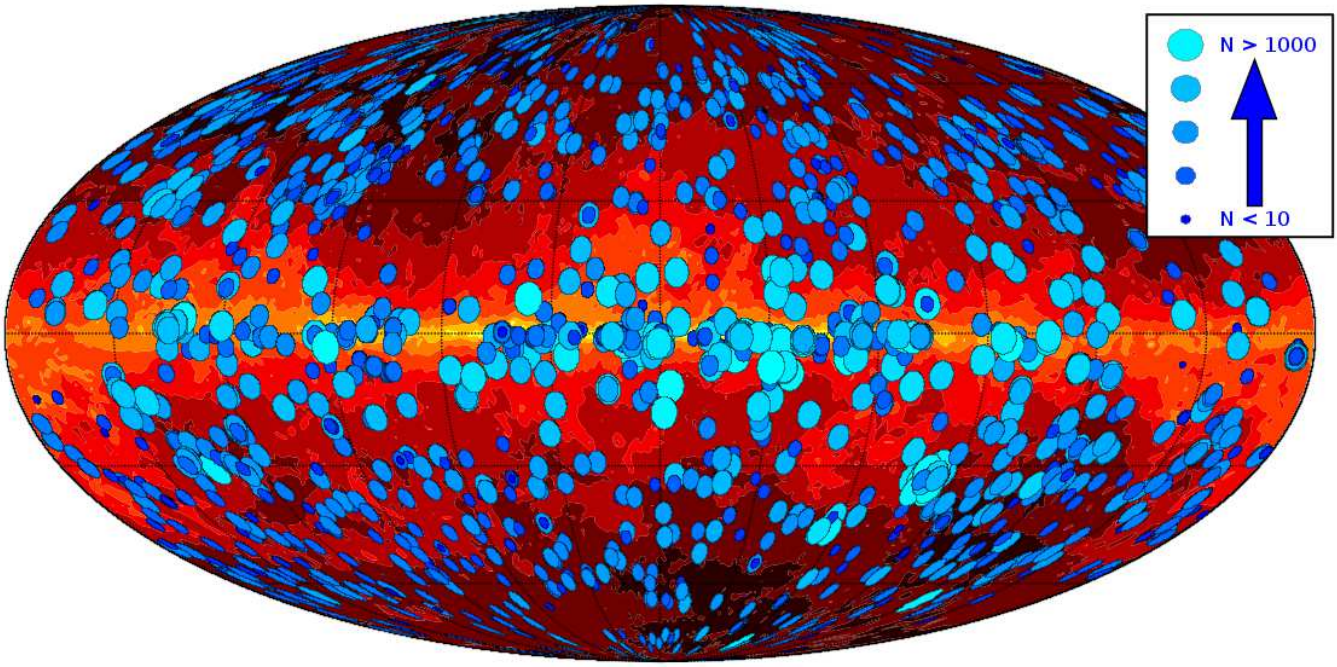

Figure 10. The pointing and source number content of the XMM-SUSS catalogue (blue circles) mapped onto a Mollweide equal area projection of the sky in Galactic longitude and latitude. Size and colour of the circles trace the total number of UV sources N in each pointing, after sources in different filters have been matched. The colour image in the background is the Infra-Red Astronomy Satellite (IRAS; Clegg 1980) 100μm all-sky map (Schlegel, Finkbeiner & Davis, 1998), showing the dust associated with our Galaxy.

Table 4. Sky coverage and source statistics for each of the six XMM-OM bandpasses included within the catalog. Ω is the solid angle accumulated by each bandpass, $N_{\rm tot}$ is the number of sources found with a detection significance $> 3\sigma$ and $f_{\rm obs}$ is the fraction of XMM-SUSS pointings that include each bandpass. $N_{\rm src}$ is the number of unique sources detected, after repeat detections are accounted for. $N_{\rm gal}$ is the number of sources within $\pm5^\circ$ of the Galactic plane, $N_{\rm mag}$ is the number of sources within a cone of radius 4°, centered around the Magellanic Clouds at $l = 278^\circ$, $b = -33^\circ$. $N_{\rm hi\text{-}b}$ is the number of objects at high Galactic latitude, $|b| > 30^\circ$, excluding the Magellanic Cloud cone.

Filter	Ω (deg^2)	$f_{\rm obs}$ (per cent)	$N_{\rm tot}$	$N_{\rm src}$	$N_{\rm gal}$	$N_{\rm mag}$	$N_{\rm hi\text{-}b}$
UVW2	43.7	15.9	119 805	96 814	25 097	50 158	24 439
UVM2	29.0	19.3	145 210	120 510	25 625	53 208	35 311
UVW1	54.0	82.0	618 266	521 507	124 188	71 948	199 934
U	21.6	23.6	177 569	146 329	34 080	4 887	74 815
B	14.3	10.8	81 191	62 966	8 738	0	42 644
V	12.6	10.4	78 160	57 498	27 366	0	23 073

spectively. The AB magnitude distributions peak at much fainter magnitudes than these conservative limits: $m_{\rm AB}$ = 20.2, 20.9 and 21.2 in UVW2, UVM2 and UVW1 respectively. For comparison, the *GALEX* All-sky Imaging Survey (AIS) reaches $m_{\rm AB} = 19.9$ and $m_{\rm AB} = 20.8$ in the FUV and NUV filters respectively, while the *GALEX* Medium Imaging Survey (MIS) reaches FUV and NUV depths of $m_{\rm AB}$ = 22.6 and 22.7, respectively (Morrissey et al., 2007).

In Fig. 13 we show the distribution of magnitude uncertainties as a function of magnitude. The solid line in each plot gives the median uncertainty, while the dashed and dotted lines indicate the 68 and 95 per cent limits of the distribution at each magnitude. To a median uncertainty of 0.1 mag, the UVW1 and U bands probe the faintest AB magnitudes (19.9 and 20.0 mag respectively). The photometric uncertainties increase significantly to fainter magnitudes, although at the faintest magnitudes the reported uncertainties may be over-conservative (see Section 4.3). At the very faintest magnitudes the shallowest (800–1000s) exposures no longer contribute any sources and the catalogue becomes dominated by sources which are detected in the longest exposures. As a result, a decrease in the median photometric uncertainty is seen in most bands at very faint magnitudes.

5.3 Time sampling

XMM-SUSS source properties can be sampled on three distinctive time scales. Multiple exposures through a particular filter are often obtained during one pointing. Depending on the length of a spacecraft visit, they provide sampling on timescales typically between hours and a day. The longest observations are curtailed by radiation constraints at the

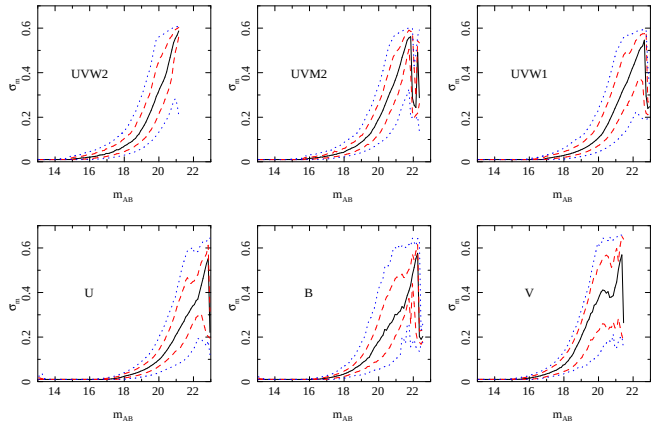

Figure 13. The distribution of magnitude uncertainties in the XMM-SUSS as a function of passband and magnitude. The solid black line shows the median error, the dashed red lines enclose 68 per cent of the distribution, and the blue dotted lines 95 per cent. The distributions were calculated in bins of 0.1 magnitude.

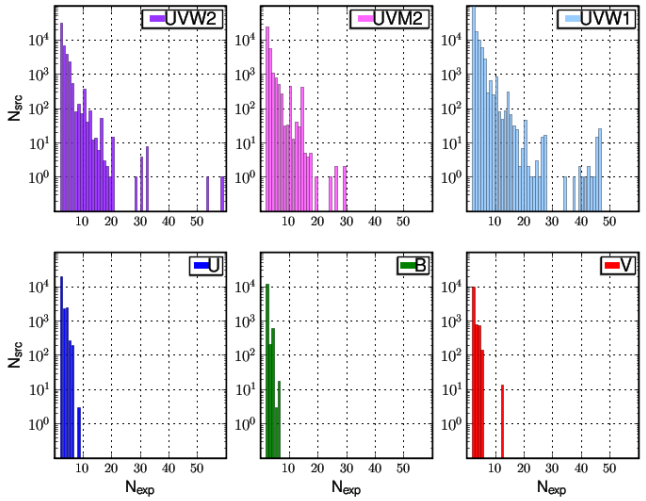

Figure 14. Distribution of source re-detections during single pointings. $N_{\rm exp}$ is the number of images taken during a single pointing in which a particular source has been detected. $N_{\rm src}$ is the number of sources detected $N_{\rm exp}$ times. Objects which are detected only once, $N_{\rm exp} = 1$, and sources with quality flags are excluded from the sample.

perigee of the 48 hour spacecraft orbit and individual exposures are limited typically to durations < 5 ksec in order to avoid potential memory corruption after cosmic ray hits. Segregated by filter, Fig. 14 illustrates the number distribution of repeat detections within individual pointings. The differences between UV and optical distributions are a consequence of data selection, where only those optical sources with UV counterparts within the catalogue are selected for inclusion. Generally speaking, if a large number of U, B or V images are being obtained, then an observing strategy has been tailored by the investigator in order to monitor variability in the optical bands, and no UV images will have been taken. For sources with multiple detections in the same filter within an *XMM-Newton* observation, XMM-SUSS contains the number of detections, the χ^2/ν for a constant countrate

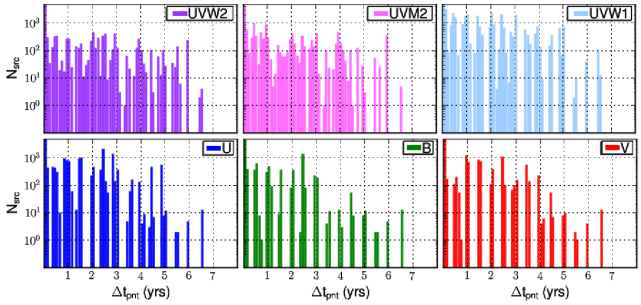

Figure 15. The number of sources $N_{\rm src}$ which are observed in multiple spacecraft pointings against the interval between the first and last detections of the source, $\Delta t_{\rm pnt}$, in units of years. Only sources without quality flags are included.

fitted to the individual measurements (ν is the number of degrees of freedom in the fit), and the maximum deviation from the median countrate in units of sigma. These latter two measurements allow the selection and identification of time-variable sources in the catalogue. For a non-varying source, χ^2/ν is expected to be approximately 1, while sources with significant variability will be inconsistent with the constant model, and so will have larger χ^2/ν.

The second timescale for source sampling is of the order of days, and is due to observations which are repeated within a few *XMM-Newton* orbits, typically to build up exposure times which are longer than can be accomodated in a single orbit. The third timescale for source sampling is of the order of years, and is associated with re-pointings towards old fields, either serendipitously or as part of a monitoring program. Fig. 15 presents the number of sources detected during more than one pointed observation, and the number of pointings in which each source is detected, against the time interval covered by the pointings. The time domain for multiple detections included in the catalog spans slightly over 8 years. The biannual sampling apparent in Fig. 15 is the result of seasonal spacecraft pointing constraints, imposed by the need to maintain the sun angle normal to *XMM-Newton's* solar panels.

The three variability timescales provide the means to search for a variety of source populations. For example, the short timescale is sensitive to accreting binaries and coronal flares in young stars. The long timescale is suitable for supernova searches and active galaxy detection. Table 5 summarizes the total number of sources with temporal information provided within the XMM-SUSS catalog.

5.4 Source colours

For XMM-SUSS sources detected through three or more filters we can produce colour-colour distributions. The two examples presented in the upper panels of Fig. 16 display the UVW2−UVM2 vs UVM2−UVW1 plane and the U−B vs B−V plane, both with distinctive sample structure. No attempt has been made to de-redden or K-correct the colours for dust extinction or cosmological redshift.

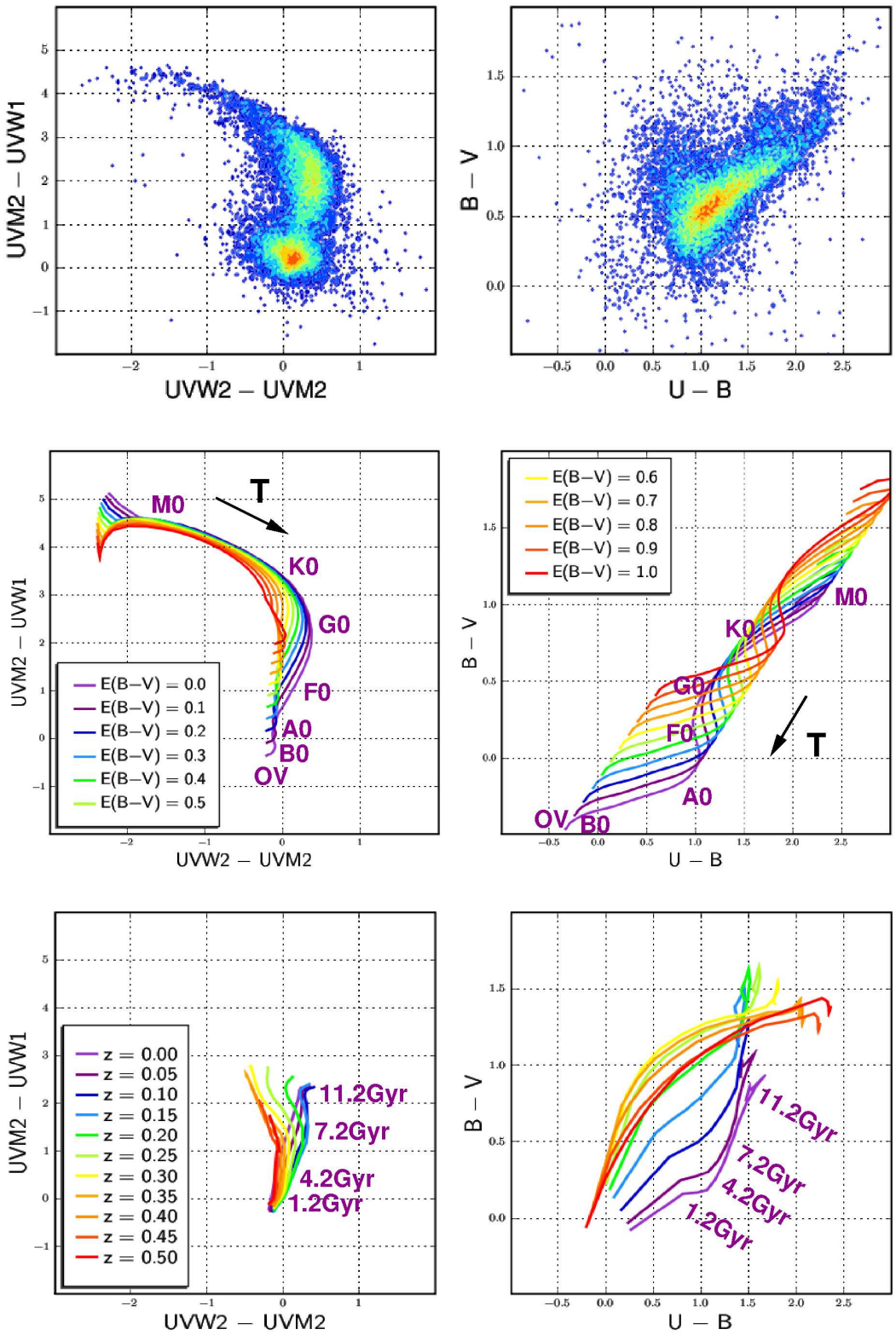

Figure 16. Top panel: UV and optical colour-colour diagrams of XMM-SUSS sources. The density scales are logarithmic. Sources with quality flags have not been included in the distributions. Middle panel: UV and optical colours derived from ATLAS9 $\log(g) = 5.0$, solar abundance stellar spectra models behind a family of Galactic dust columns where $E\,(\mathrm{B-V}) = 0.0$–1.0 and $R_{\mathrm{V}} = 3.08$. The arrows indicate the direction of increasing stellar temperature along the tracks, and spectral types are indicated on the zero-reddening tracks. Bottom panel: galaxy colours from the E/S0 evolutionary models of Rocca-Volmerange (1988) with a range of ages from 0.2 to 13.2 Gyr at redshifts of $0.0 < z < 0.5$. Ages are indicated on the zero-redshift tracks.

Table 5. Counting statistics for sources detected in multiple images. Nexp is the total number of sources detected in more than one exposure through a specific filter and during a single spacecraft pointing. $f_{\rm exp}$ is the fraction of sources detected more than once per pointing per filter. $N_{\rm obs}$ is the total number of sources detected multiple times during different spacecraft pointings. $f_{\rm obs}$ is the fraction of unique sources detected during different pointings.

Filter	Nexp	$f$exp (per cent)	$N_{\rm obs}$	$f_{\rm obs}$ (per cent)
UVW2	46,031	38.4	11,657	12.0
UVM2	33,660	23.2	13,010	11.8
UVW1	137,309	22.2	58,280	11.2
U	24,627	13.9	18,625	12.7
B	12,732	15.7	9,702	15.4
V	1,724	15.0	12,022	20.9

5.4.1 Stellar colours

To examine the colours of stars in the XMM-OM bandpasses we make use of synthesized stellar spectra, computed from 910–10 000Å and binned to 20Å, provided by the ATLAS9 project (Castelli & Kurucz, 2003) using Grevesse & Sauval (1998) abundances. In the middle panel of Fig. 16 we show the ATLAS9 $\log(g) = 5.0$ stellar sequence, extinguished with a range of Galactic dust columns, and folded through the XMM-OM effective area curves (Fig. 1). The minimum photospheric temperature represented is 3 000K, the hottest is 50 000K. We use the analytical approximation to the Galactic dust extinction curve described by Pei (1992) and characterize the dust columns by the colour excess E(B−V). The arrows indicate the approximate direction of increasing photospheric temperature along the tracks. In optical colours, the stellar tracks are easily understood with stars revealing ever-bluer colours, right-to-left and top-to-bottom as we travel from cool M to hot O stars. The UV colours reveal a different trend however: cool stars are located in the top left of the plot, with UVW2-UVM2 colours increasing (i.e. moving to the right) as temperature increases from M stars to hotter types before turning a corner at approximately solar spectral types. This cool-star trend is a consequence of them having negligible UV flux while the red wing of the UVW2 transmission curve[7] extends deeper into the optical bands than that of UVM2 (Talavera, 2011). Consequently more photons are collected from K and M stars through UVW2 than UVM2.

UVM2−UVW1 colours evolve monotonically towards larger values as dust extinction increases. UVW2−UVM2 colours do not and there are two contributary factors to this. The first is that the broad 2 175Å graphite feature has most effect in the UVM2 band. Increasing extinction will deplete UVM2 photons faster than UVW2 photons. Secondly, cool stars emit very few photons in the UV bands. Those photons which are detected from M and K stars leak in through the red wings of the filters reponses, the UVW2 filter being more efficient than UVM2 in these wings. There is degeneracy in the UV colours between M dwarfs and for example highly reddened G stars so Galactic extinction must be taken into account before identifying cool stars, but critically there is little degeneracy between the effects of dust extinction and the intrinsic colours of hot stars.

The UV stellar loci shown in the middle panel of Fig. 16 are mirrored faithfully in the real catalogue shown in the top panel. The distribution of sources indicates that the bulk of the stellar population shown in this panel are stars of spectral-type G or earlier, with moderate interstellar reddening (E(B − V) < 0.3). This is not surprising, because XMM-SUSS sources must be detected in all 3 of the XMM-OM UV bandpasses to appear on the UV colour-colour diagram.

Predictably, the effects of dust extinction on the optical colours, where the extinction curve is featureless and the wings of the filters are not an important issue, are more simple. As the B−V colour excess increases, the U−B colour becomes more red. Clearly, owing to several knees in the stellar curve, there is more significant extinction degeneracy in optical colours than in UV colours in the region containing the majority of optical XMM-SUSS sources.

5.4.2 Galaxy colours

To examine the colours of galaxies in the XMM-OM bandpasses we have used synthetic galaxy spectra from the template library of Rocca-Volmerange (1988). The templates have an exponentially-declining star formation law (the template family "UV-cold E/S0" in Rocca-Volmerange (1988)) and a range of ages from 0.2 to 13.2 Gyr, i.e. from strongly star-forming to old-star dominated. The spectra were redshifted out to $z = 0.5$ in discrete steps and folded through the XMM-OM bandpasses. The synthetic tracks so produced are shown in the bottom panels of Fig. 16, colour coded by redshift.

In the UV colour-colour plot, the tracks corresponding to different redshifts have a larger extent in the UVM2−UVW1 colour than in UVW2−UVM2. They separate at the red end of the sequence, but converge at the blue end: blue, star-forming galaxies at all redshifts out to $z = 0.5$ have UV colours UVM2−UVW1 ≈ UVW2−UVM2 ≈ 0. In the top-left panel of Fig. 16 it is seen that there is a dense cloud of XMM-SUSS sources, corresponding to blue, star-forming galaxies, at this location in the UV colour-colour plane. The association of this cloud with galaxies is confirmed when we note that 85 per cent of the sources in this plot, which are flagged as extended in UVW1, lie in this cloud, with UVM2−UVW1< 1, while the majority of point-like sources have UVM2−UVW1> 1. However, it should be noted that the hot end of the stellar locus extends into this same region of the UV colour-colour plane as the galaxies, so that the UV colours alone cannot be used to separate stars and galaxies as reliably as the combinations of UV and SDSS colours used by (Bianchi et al., 2007, 2011).

The optical colours of the synthetic galaxies evolve towards the top-left of the U−B vs B−V diagram in the interval $0.00 < z < 0.35$ as the Balmer break moves through the B band. At redshifts $z > 0.35$ the Balmer break moves into the V band and the trend is reversed. The spur of XMM-SUSS sources in the top-right panel of Fig. 16 with U−B ≈ 0.7 and 0.5 <B−V< 1.0 suggests that many XMM-SUSS galaxies have $z > 0.2$.

[7] Longward of 3 000Å, both the UVW2 and UVM2 filters have < 0.1 per cent transmission, and hence their red tails are too weak to be seen in Fig. 1

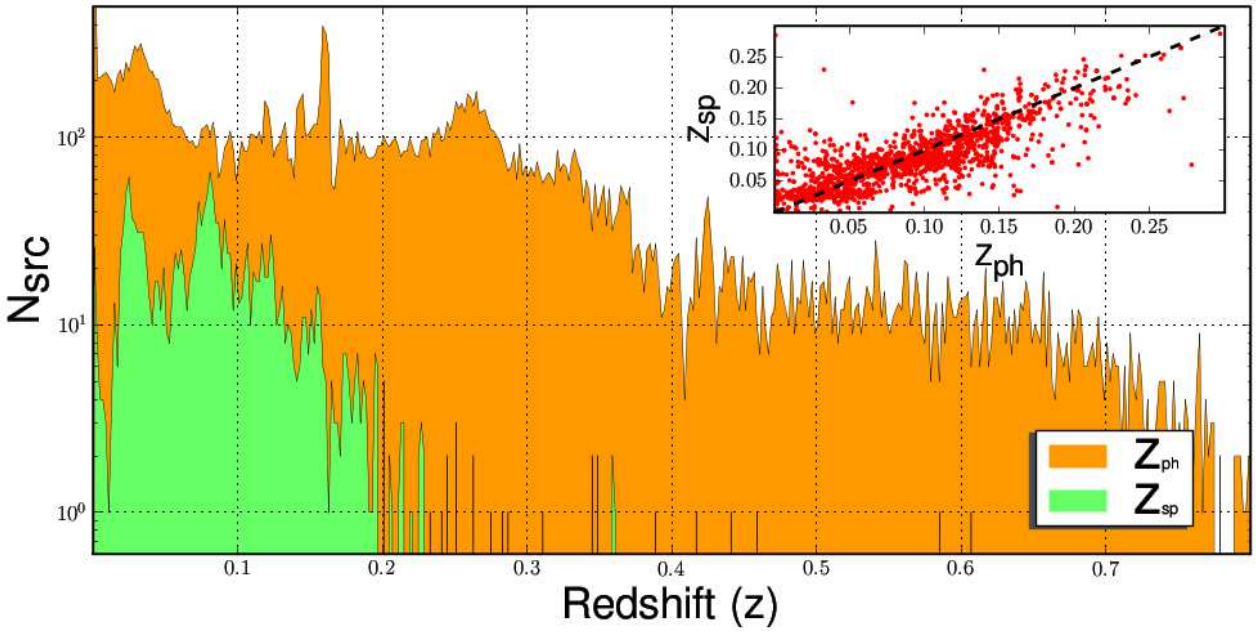

Figure 17. Distribution of SDSS photometric (orange) and spectroscopic (green) redshifts of SDSS DR6 counterparts to XMM-SUSS sources. The histogram is sampled in bins of width $\Delta z = 2 \times 10^{-3}$. The inset provides the photometric-to-spectroscopic distribution of sources where a redshift has been measured by both methods.

5.5 Redshift distribution

The redshift distribution of XMM-SUSS galaxies bears heavily on their utility for extragalactic science. The redshift distribution can be obtained by cross-correlation of the XMM-SUSS with galaxies from the SDSS DR6 catalogue (Adelman-McCarthy et al., 2008), which includes many spectroscopic redshifts, and a much larger number of photometric redshifts. The catalogues were matched by searching for the nearest clean XMM-SUSS source within 2 arcsec of an SDSS galaxy. The redshift distributions of XMM-OM sources with SDSS DR6 galaxies are shown in Fig. 17. It suggests that the majority of XMM-SUSS galaxies have $z < 0.4$, but with a significant minority lying at $0.4 < z < 0.8$. The spectroscopic redshift limit at $z = 0.2$ is a systematic feature of the SDSS rather than intrinsic to the XMM-SUSS sample. It is not clear how accurate the SDSS photometric redshifts are for UV-selected sources at the sample limit of $z \sim 0.8$, although the correlation between photometric and spectroscopic SDSS redshifts within the inset of Fig. 17 indicates that photometric redshifts can be trusted to within a few 10^{-2} over $0.0 < z < 0.25$.

5.6 Synergy with 2XMM

As the XMM-OM data used to construct the XMM-SUSS were obtained simultaneously with X-ray imaging data from the European Photon Imaging Camera instruments (EPIC; Turner et al., 2001; Strüder et al., 2001) the XMM-SUSS is a useful resource for studying the UV and optical properties of X-ray sources. In this context, the 2XMM catalogue of X-ray sources detected serendipitously in EPIC images (Watson et al., 2009) is the natural X-ray catalogue to pair with the XMM-SUSS and some results from matching the two catalogues have already been published (Vagnetti et al., 2010).

The current version of XMM-SUSS does not contain cross-references to X-ray sources in 2XMM, so the user will have to carry out his or her own cross matching, the parameters of which will depend on the details of the scientific investigation being carried out. To examine the potential sample size for joint 2XMM – XMM-SUSS studies, we have applied a simple cross-match between 2XMM-DR3 catalogue and XMM-SUSS using a maximum distance of 5 arcsec. We obtain 14 275 matches, and we estimate[8] that 90 per cent of these will be genuine associations.

6 COMPARISON WITH OMCAT

An alternative catalogue of XMM-OM sources (OMCat, Kuntz et al., 2008), constructed and released independently of the XMM-SUSS, is available through the HEASARC and the Multimission Archive at STScI (MAST). Here we outline the most important differences between XMM-SUSS and OMCat.

In scope, the two catalogues differ significantly. The XMM-SUSS is a catalogue of UV-detected sources, i.e. it contains only sources detected in one or more of the UVW1, UVM2 and UVW2 bandpasses, whereas the OMCat is a catalogue of XMM-OM sources detected in any of the XMM-OM optical and UV bandpasses. The OMCat was constructed using *XMM-Newton* observations available in the

[8] We estimate the spurious match rate by cross matching the two catalogues at 5–10 arcsec offsets, noting that almost all genuine counterparts will be offset by less than 5 arcsec (Pineau et al., 2011).

public archive on 1 September 2006, a somewhat earlier cut-off date than the XMM-SUSS bearing in mind the 1-year proprietary period. Obvious problem fields were screened out of the XMM-SUSS (Section 2.2), but were not excluded from the OMCat. The OMCat contains a larger total number of sources (947 638) than the XMM-SUSS, but only around half as many UV-detected sources (364 741) as the XMM-SUSS. The increased number of UV sources in the XMM-SUSS relative to the OMCat partly results from the expansion of the archive and partly from improvements in the source detection chain between the construction of OMCat and the XMM-SUSS: the peaks in the UV magnitude distributions of XMM-SUSS sources are more than half a magnitude fainter than those in OMCat.

Both the XMM-SUSS and OMCat were generated primarily using the *XMM-Newton* SAS tasks to process XMM-OM imaging data. The OMCat was produced using the tasks in SAS version 6.5.0, whereas the XMM-SUSS was produced using the tasks in SAS version 8.0. Significant improvements were made between these two versions, in part driven by the requirements for the XMM-SUSS catalogue. These improvements include a more robust detection scheme for sources close to the limit of sky background, better discrimination between point-like and extended sources, correction for the time-dependent degradation of the XMM-OM sensitivity, more comprehensive quality flagging and a higher success rate (90 per cent) for refined aspect corrections. Notably, for the construction of the OMCat a bespoke aspect correction process was developed and employed to achieve acceptable astrometry in the catalogue. For the XMM-SUSS, no further aspect correction was required beyond the refined aspect corrections derived within the SAS version 8.0 processing.

7 KNOWN ISSUES WITH THE XMM-SUSS AND PLANS FOR IMPROVEMENT

We briefly describe a number of known problems and issues with the XMM-SUSS, and improvements we are planning for future versions of the catalogue. The XMM-OM instrument team intends to improve and enlarge the XMM-SUSS on a regular basis, depending on available resources.

7.1 Very extended sources

Very large extended sources which occupy a significant fraction of the XMM-OM field of view (including for example M 31 and the Crab nebula), were not systematically screened from the input data for the XMM-SUSS. The XMM-OM source detection algorithm was not designed to deal with such large sources, which it treats as non-uniform background, and a large fraction of the detected sources in these images are spurious. The resultant source lists are not, however, crowded enough to be excluded from the catalogue by the source density criterion described in Section 2.2. We intend to screen such fields from future versions of the catalogue.

7.2 Photometry of point and extended sources

Sources which are marginally resolved may be identified in some observations as extended, but be classified as point-like in other observations. Because photometry is computed in a different manner for point and extended sources, this can lead to inconsistent photometry between observations, when a source is not intrinsically variable. We advise users of the catalogue to check that sources which appear to vary between observations have consistent morphological classifications in the different observations before concluding that they are variable. In future versions of the catalogue, we intend to provide aperture photometry for all sources, in addition to extended-source photometry for extended sources, to rectify this issue.

7.3 Lower limits for non-detections are not provided

In the present catalogue, when a source is not detected in a particular filter it is not possible to distinguish the cases in which the source is not detected because it is too faint in that filter, because no exposure was taken in that filter, or because the exposures in that filter were not used in the catalogue due to source crowding. Furthermore it would be useful to provide the specific background limit for sources which are not detected in some filters. However, the functionality to perform aperture photometry over the positions of these non-detected sources is not currently within the pipeline. This functionality is a desirable feature for future versions of the XMM-SUSS.

7.4 Over-conservative photometric uncertainties at faint magnitudes

As shown in Section 4.3 the photometric scatter obtained from multiple observations of sources falls below the measurement errors for measurement errors larger than 0.1 mag in all filters, implying that photometric uncertainties > 0.1 mag reported in the catalogue are probably larger than the real photometric uncertainties. It follows that the variability indicators (χ^2/ν amd maximum deviation in units of σ; columns 80–91, described in Appendix C) will be underestimated for objects which have photometric errors > 0.1 mag. We intend to diagnose and rectify this problem before the next release of the catalogue.

7.5 Detections of the same source in different observations are sometimes not matched

We are aware of some cases in which a single source has been detected in more than one *XMM-Newton* observation, but is treated as though it were more than one source within the catalogue (i.e. the different detections are assigned different SRCNUM values). The cause of this problem is under investigation.

7.6 Accuracy of coincidence loss in extended sources is unquantified

Corrections for coincidence loss are essential for photometry of bright sources. Using photometric standards the effect has

been well-calibrated in point sources, but the calibration has not been tested upon bright extended sources. This is rarely an issue for extended sources in the UV, because the coincidence loss correction is usually small, but for the optical pass bands it can be significant. Events from an extended source will have a different positional distribution compared to a point source, and hence the coincidence loss will differ. The coincidence-loss correction of extended sources therefore comes with an unquantified systematic error.

7.7 Area over which photometry is integrated for extended sources is not given

Information on the area over which the flux is integrated in extended-source photometry is not preserved in the catalogue. Such information may be useful when comparing the XMM-OM photometry to photometry from other sources. As such, it would be advantageous to provide this information in a future version of the catalogue.

7.8 Other planned improvements to future releases

The current version of the XMM-SUSS was obtained by source-searching individual XMM-OM exposures and merging the resulting source lists. Functionality to aspect-correct and stack the XMM-OM images prior to source detection has now been built into the XMM-OM SAS tasks, and will be used in future versions of the catalogue. Furthermore, a significant number of *XMM-Newton* observations have been performed since the cut-off date for the current XMM-SUSS catalogue. Substantial increases in both sky area and depth are therefore anticipated in the next version of the catalogue.

8 CONCLUSIONS

We have described the construction, validation, and characteristics of the XMM-SUSS, a catalogue of UV sources detected with the XMM-OM. The catalogue contains source positions and magnitudes in up to 6 UV and optical bands, profile diagnostics and variability statistics. The XMM-SUSS contains 753 578 UV source detections which, taking into account repeat observations of the same patches of sky, relate to 624 049 unique objects. Taking into account overlaps between *XMM-Newton* observations, the sky area covered is 29-54 deg^2 depending on UV filter. The catalogue includes observations at a wide range of Galactic latitudes, including the Galactic plane. In terms of depth, the catalogue is typically deeper than the *GALEX* All-sky Imaging Survey: the AB magnitude distributions peak at $m_{\rm AB}$ = 20.2, 20.9 and 21.2 in UVW2, UVM2 and UVW1 respectively. The magnitude limits are not uniform over the survey, depending on background level and exposure time. However, we estimate that all fields are complete for magnitudes brighter than $m_{\rm AB}$ = 18.1, 18.8 and 19.4 in UVW2, UVM2 and UVW1 respectively. We show that the catalogue is rich in early-type stars, and star-forming galaxies out to a redshift of 0.8. The catalogue has been extensively tested for quality in astrometry, photometry and reliability. The XMM-SUSS has significant potential for science based on temporal source variability on timescales of hours to years, because a large fraction of sources (38 per cent in UVW2, 23 per cent in UVM2 and 22 per cent in UVW1) have been observed multiple times through the same filter within an *XMM-Newton* pointing, and a significant fraction of sources (12 per cent in UVW2 and 11 per cent in UVM2 and UVW1) have been detected in multiple *XMM-Newton* pointings. The XMM-SUSS catalogue provides a useful resource for a wide range of scientific applications, whether for statistical studies (e.g. Vagnetti et al., 2010), or simply as a convenient source of UV/optical photometry for small samples of objects (e.g. Jin et al., 2012) or individual sources (e.g. Smith, Page & Branduardi-Raymont, 2009).

ACKNOWLEDGMENTS

This research has made use of the following archives: the USNOFS Image and Catalogue Archive operated by the United States Naval Observatory, Flagstaff Station; the Two Micron All Sky Survey, which is a joint project of the University of Massachusetts and the Infrared Processing and Analysis Center/California Institute of Technology, funded by the National Aeronautics and Space Administration and the National Science Foundation. We thank Tom Dwelly for supplying the Subaru B band image and sourcelist for the 13^H deep field.

REFERENCES

Adelman-McCarthy J. K., Agüeros M. A., Allam S. S., Allende Preito C., Anderson K. S. J., Anderson S. F., Annis J., Bahcall N. A., et al., 2008, ApJS, 175, 297

Albrecht R. & Jakobsen P., 2002, Space Telescope European Coordinating Facility Newsletter, 31, p.6

Antokhin I., 2001, Technical Report XMM-SOC-TN-0015, Photometric Accuracy of the Optical Monitor, ESA

Bertin E., & Arnouts S., 1996, A&AS, 117, 393

Bianchi L., Rodriguez-Merino L., Viton M., Laget M., Epremova B., Herald J., Conti A., Shiao B., et al., 2007, ApJS, 173, 659

Bianchi L., Efremova B., Herald J., Girardi L., Zabot A., Marigo P., Martin C., 2011, MNRAS, 411, 2770

Boggess A., Bohlin R. C., Evans D. C., Freeman H. R., Gull T. R., Heap S. R., Klinglesmith D. A., Longanecker G. R., Sparks W., West D. K., Holm A. V., Perry P. M., Schiffer F. H., Turnrose B. E., Wu C. C., Lane A. L., Linsky J. L., Savage B. D., Benvenuti P., Cassatella A., Clavel J., Heck A., Macchetto F., Penston M. V., Selvelli P. L., Dunford E., Gondhalekar P., Oliver M. B., Sandford M. C. W., Stickland D., Boksenberg A., Coleman C. I., Snijders M. A. J., Wilson R., 1978, Nature, 275, 377

Bohlin R. C., 2007, in Sterken C., ed., The Future of Photometric, Spectrophotometric and Polarimetric Standardization, Astronomical Society of the Pacific Conference Series, 364, 315

Boksenberg A., Evans R. G., Fowler R. G., Gardner I. S. K., Houziaux L., Humphries C. M., Jamar C., Macau D., Malaise D., Monfils A., Nandy K., Thompson G. I., Wilson R., Wroe H., 1973, MNRAS, 163, 291

Bowyer S., Sasseen T. P., Lampton M., Wu X. 1993, ApJ, 415, 875

Carruthers P., 1973, Applied Optics, 12, 2501
Castelli F., Kurucz R. L., 2003, in Piskunov N., Weiss W. W., Gray D. F., eds, Modelling of Stellar Atmospheres, IAU Symposium Series, 210, 20
Clegg P.E., 1980, Phys. Scr., 21, 678
Code A.D., Houck T.E., McNall J.F., Bless R.C., Lillie C.F., 1970, ApJ, 161, 377
Davis R. J., Deutschman W. A., Lundquist C. A., Nozawa Y., Bass S. B., 1972, *Scientific results from the Orbiting Astronomical Observatory (OAO-2)* Proceedings of a Symposium, held in Amherst, Mass., August 23-24, 1971, Washington: NASA, 1972, ed. Code, A. D., p.1
de Jager C., Hoekstra R., van der Hucht K. A., Kamperman T. M., Lamers H. J., Hammerschlag A., Werner W., Emming J. G., 1974, Ap&SS, 26, 207
Drory N., 2003, A&A, 397, 371
Ehle M., de la Calle I., Díaz Trigo M., González Riestra R., Loiseau N., Rodriguez P., 2008, XMM-Newton Users Handbook, ESA
Fälker J., Gordon F., Sandford M. C. W., 1987, in Kondo Y. ed., Exploring the Universe with the IUE Satellite, Astrophysics and Space Science Library, 129, 21
Fordham J. L. A., Bone D. A., Read P. D., Norton T. J., Charles P. A., Carter D., Cannon R. D., Pickles A. J., 1989, MNRAS, 237, 513
Fordham J. L. A., Moorhead C. F. & Galbraith R. F., 2000, MNRAS, 312, 83
Grevesse N., Sauval A. J., 1998, Space Science Reviews, 85, 161
Guainazzi M., Santos-Lleó M., 2004, XMM Data Files Handbook, XMM-SAX-VILSPA/2000-0109 edn, ESA
Henry R. C., Weinstein A., Feldman P. D., Fastie W. G., Moos H. W., 1975, ApJ, 201, 613
Henize K. G., Wray J. D., Parsons S. B., Benedict G. F., Bruhweiler F. C., Rybski P. M., O'Callaghan F. G., 1975, ApJ, 199, L119
Jin C., Ward M., Done C., Gelbord J., 2012, MNRAS, 420, 1825
Johnson H. L. & Morgan W. W., 1951, ApJ, 114, 522
Kawakami H., Bone D., Fordham J., Michel R., 1994, Nuclear Instruments and Methods in Phys. Res. A, 348, 707
Kimble R.A., Woodgate B.E., Bowers C.W., Kraemer S.B., Kaiser M.E., Gull T.R., Heap S.R., Danks A.C., et al., 1998, ApJ, 492, L83
Kirsch M. G. F., Altieri B., Chen B., Haberl F., Metcalfe L., Pollock A. M., Read A. M., Saxton R. D., et al., 2004, in Hasinger G., Turner M. J. L., eds, Society of Photo-Optical Instrumentation Engineers (SPIE) Conference Series, 5488, 103
Kuin N. P. M. & Rosen S. R., 2008, MNRAS, 383, 383
Kuntz K. D., Harrus I., McGlynn T. A., Mushotzky R. F., Snowden, S. L., 2008, PASP, 120, 740
Lasker B. M., Lattanzi M. G., McLean B. J., Bucciarelli B., Drimmel R., Garcia J., Greene G., Guglielmetti F., et al., 2008, AJ, 136, 735
Landolt A. U., 1992, AJ, 104, 340
MacKenty J.W., Kimble R.A., O'Connell R.W., Townsend J.A., 2010, in Oschmann, J.M., Clampin M.C., MacEwan H.A., eds, Society of Photo-Optical Instrumentation Engineers (SPIE) Proceedings, 7731, 27
Mason K. O., Breeveld A., Much R., Carter M., Cordova F. A., Cropper M. S., Fordham J., Huckle H., Ho C., Kawakami H., Kennea J., Kennedy T., Mittaz J. P. D., Pandel D., Priedhorsky W. C., Sasseen T., Shirey R., Smith P., Vreux J. -M., 2001, A&A, 365, L36
Martin D. C., Fanson J., Schiminovich D., Morrissey P., Friedman P. G., Barlow T. A., Conrow T., Grange R., Jelinsky P. N., Milliard B., Siegmund O. H. W., Bianchi L., Byun Y-I., Donas J., Forster K., Heckman T. M., Lee Y-W., Madore B. F., Malina R. F., Neff S. G., Rich R. M., Small T., Surber F., Szalay A. S., Welsh B., Wyder T. K., 2005, ApJ, 619, 1
Monet D. G., Levine S. E., Canzian B., Ables H. D., Bird A. R., Dahn C. C., Guetter H. H., Harris H. C., et al., 2003, AJ, 125, 984
Morrissey P., Conrow T., Barlow T. A., Small T., Seibert M., Wyder T. K., Budavári T., Arnouts S., et al., 2007, ApJS, 173, 682
Pei Y. C., 1992, ApJ, 395, 130
Pineau F.-X., Motch C., Carrera F., Della Ceca R., Derrièe S., Michel L., Schwope A., Watson M.G., 2011, A&A, 527, 126
Rocca-Volmerange B., Guiderdoni B., 1988, A&AS, 75, 93
Roming P. W. A., Kennedy T. E., Mason K. O., Nousek J. A., Ahr L., Bingham R. E., Broos P. S., Carter M. J., et al., 2005, Space Science Reviews, 120, 95
Schlegel D. J., Finkbeiner D. P. & Davis M., 1998, ApJ, 500, 525
Seymour N., Dwelly T., Moss D., McHardy I., Zoghbi A., Rieke G., Page M., Hopkins A., et al., 2008, MNRAS, 386, 1695
Sirianni M., Jee M.J., Benítez N., Blakeslee J.P., Martel A.R., Meurer G., Clampin M., De Marchi G., et al., 2005, PASP, 117, 1049
Smith R.A.N., Page M.J., Branduardi-Raymont G., 2009, A&A, 490, 103
Stecher T. P., Cornett R. H., Greason M. R., Landsman W. B., Hill J. K., Hill R. S., Bohlin R. C., Chen P. C., Collins N. R., Fanelli M. N., Hollis J. I., Neff S. G., O'Connell R. W., Offenberg J. D., Parise R. A., Parker J., Roberts M. S., Smith A. M., Waller W. H., 1997, PASP, 109, 584
Stetson P. B., 2000, PASP, 112, 925
Still M., Brindle C., Page M., Yershov V., Breeveld A., Ziaeepour H., Rosen S., Talavera A., 2008, "The X-ray Universe 2008" Symposium held in Granada, Spain, 27-30 May, 2008; Published online at http://xmm.esac.esa.int/external/xmm_science/ workshops/2008symposium, p.122
Strüder L., Briel U., Dennerl K., Hartmann R., Kendziorra E., Meidinger N., Pfeffermann E., Reppin C., Aschenbach B., et al., 2001, A&A, 365, L18
Talavera A., 2011, Technical Report XMM-SOC-CAL-TN-0019 issue 6.0, *XMM-Newton* Optical and UV monitor (OM) Calibration Status, ESA; http://xmm2.esac.esa.int/docs/documents/CAL-TN-0019.pdf
Turner M. J. L., Abbey A., Arnaud M., Balasini M., Barbera M., Belsole E., Bennie P. J., Bernard J. P., et al., 2001, A&A, 365, L27
Trauger J.T., Ballester G.E., Burrows C.J., Casertano S., Clarke J.T., Crisp D., Evans R.W., Gallagher J.S., et al., 1994, ApJ, 435, L3
Vagnetti F., Turriziani S., Trevese D., Antonucci M., 2010, A&A, 519, 17

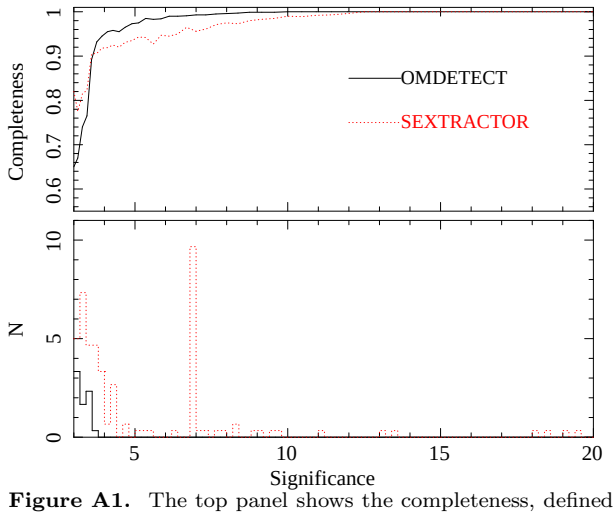

Figure A1. The top panel shows the completeness, defined by (number of matched test sources)/(number of test sources), of OMDETECT and SEXTRACTOR in trials with simulated XMM-OM images as a function of source significance. The lower panel shows the number of spurious sources detected per 1000 fields as a function of source significance, from running OMDETECT and SEXTRACTOR on 3000 simulated source-free fields.

van Duinen R. J., Aalders J. W. G., Wesselius P. R., Wildeman K. J., Wu C. C., Luinge W., Snel D., 1975, A&A, 39, 159

Watson M.G., Auguères J.-L., Ballet J., Barcons X., Barret D., Boer M., Boller Th., Bromage G.E., et al., 2001, A&A, 365, L51

Watson M.G., Schröder A. C., Fyfe D., Page C. G., Lamer G., Mateos S., Pye J., Sakano M., et al., 2009, A&A, 493, 339

York D. G., Adelman J., Anderson J. E., Anderson S. F., Annis J., Bahcall N. A., Bakken J. A., Barkhouser R., et al., 2000, AJ, 120, 1579

APPENDIX A: TESTING AND VALIDATION OF THE OMDETECT SOURCE DETECTION ALGORITHM

A.1 Tests of the source detection algorithm on simulated images

The performance of the OMDETECT source detection algorithm was tested extensively on simulated data during the development cycle leading up to the construction of the XMM-SUSS. To benchmark its performance, 100 simulated images were produced with random background levels between 0 and 200 counts per pixel and sources were placed at random positions on the image. Sources were either point-like, in which case the source was constructed using the XMM-OM empirical point-spread function for a given OM filter, or extended, in which case the source had a 2-d Gaussian profile with a random position angle. The brightness distribution of the sources was generated randomly to simulate a true image. Each image had Poissonian noise added.

The input test sources were matched with those detected by OMDETECT to form a list of the properties of matched and unmatched test sources. The output sources were then checked against the input sources to ensure that the source positions, count rates, extension flags, extended source widths and orientations are correctly recovered by OMDETECT. The simulation process was also used to check the detection completeness, defined by (number of matched test sources)/(number of test sources). The top panel of Fig. A1 shows the completeness of OMDETECT derived from the simulations as a function of source significance. Comparison of the input and recovered source lists indicate that the source detection algorithm is > 95 percent complete at a signal to noise level of 5, and 100 percent complete at a signal to noise ratio of 10. As a measure of performance, the results were compared to those obtained by running SEXTRACTOR (Bertin & Arnouts, 1996), with parameters tuned for the XMM-OM images, on the same simulated images. As can be seen in Fig. A1, the completeness of OMDETECT compares favourably with that of SEXTRACTOR.

Tests of the source detection were also carried out on source-free simulated images to assess the level of spurious sources. The results of applying OMDETECT and SEXTRACTOR to 3000 simulated source-free images are shown in the lower panel of Fig. A1. Again, OMDETECT compares favourably with SEXTRACTOR.

A.2 Tests of the source detection algorithm on XMM-OM images

Prior to the construction of the XMM-SUSS, OMDETECT and SEXTRACTOR were run on a large number of OM images, and the fidelity of the two source detection algorithms were visually examined by overlaying the detected source regions on the images and looking for missed, spurious and misclassified sources. In agreement with the simulations, OMDETECT misses few sources, and those that are missed nearly always have low signal-to-noise ratios (<4) and are usually close to much brighter sources. In comparison, SEXTRACTOR generated significant numbers of spurious sources in scattered light features and coincidence-loss-induced modulo-8 distortion around bright sources, and in images with very low backgrounds.[9]

In order to provide a more quantitative validation of the fidelity of the OMDETECT source detection algorithm against an independent reference set, its performance on a 5 ksec B-filter exposure of the field centered on RA = $13^{\rm h}$ $34^{\rm m}$ $40^{\rm s}.19$, Dec = $+37^\circ$ $54\prime$ $58\farcs9$ (J2000) was compared to a deeper, independent source list. This particular field is the 13^H *XMM-Newton/Chandra* Deep Field and the independent source list was obtained using SExtractor2.5.0 (Bertin & Arnouts, 1996) from a Johnson B exposure obtained by the 8-m Subaru telescope (Seymour et al., 2008, Dwelly et al., in prep). The XMM-OM and Subaru images are shown in Fig. A2. The point spread function of the Subaru image has a full-width half-maximum of 0.87 arcsec and reaches to much fainter magnitudes than the XMM-OM image. The Subaru image covers a larger sky area than the XMM-OM image, so the Subaru source list was screened to remove objects that are outside the XMM-OM field-of-view. Sources were matched between the two catalogues using the simple criterion of nearest source within 3 arcseconds.

The left hand panel of Fig. A3 compares the B magnitudes of the XMM-OM sources with their nearest counterparts in the Subaru list, while the right hand panel shows

[9] It should be noted that SEXTRACTOR was not designed to cope with any of these image characteristics.

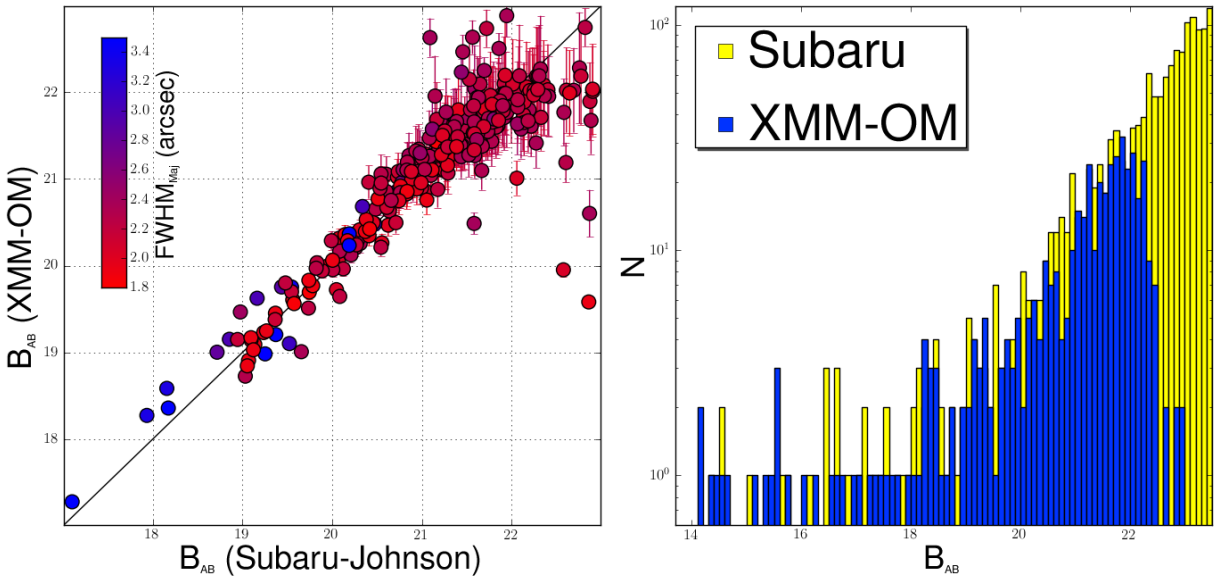

Figure A3. The left panel compares the B magnitudes of XMM-OM sources with their B Subaru counterparts. The Subaru filter is Johnson B, but the XMM-OM magnitudes have not been transformed to Johnson B because the accompanying XMM-OM data in U and V do not go sufficiently deep to facilitate this for the faintest sources. Sources have been matched between the two catalogues using the simple criteria of nearest source within 3 arcsec. Colour coding is a function of source extent on the sky, point sources are red, extended sources are blue. Error bars correspond to 1σ confidence for the XMM-OM magnitudes. The right hand panel provides a histogram of XMM-OM and Subaru source magnitudes.

the magnitude distributions of the XMM-OM and Subaru source lists. Stars with $B_{AB} < 19$ mag are not used in the photometry comparison because they are saturated in the Subaru image. The sources show a linear relation between Subaru and XMM-OM magnitudes; outliers at faint magnitudes come primarily from mis-identifications arising from the simplistic cross-matching rather than photometric variability. The Subaru and XMM-OM magnitude distributions indicate good detection consistency between the two instruments. All the Subaru objects with $B_{AB} < 19$ are detected by OMDETECT in the XMM-OM image, although with different magnitudes because of the saturation in the Subaru image. Furthermore, although there appears to be a small deficit of XMM-OM sources between $20.5 < B_{AB} < 20.9$, all of these Subaru objects are detected by OMDETECT, with slightly different magnitudes. The XMM-OM sourcelist is highly complete to $B_{AB} = 21.9$, corresponding to a signal to noise ratio of 4.5 for compact sources. Comparison with the Subaru image indicates that the source detection process works well, and corroborates the high completeness levels obtained in the simulations described at the beginning of this section.

APPENDIX B: CRITERIA USED FOR QUALITY FLAGS 1,2,3 AND 4

Here we describe the criteria used in the XMM-SUSS pipeline to identify and flag readout streaks (flag 1), smoke rings (flag 2), diffraction spikes (flag 3) and coincidence-loss distorted sources (flag 4), as described in Section 3.9.

B.1 Flag 1: readout streak

Any point-source with a raw count-rate $\geqslant 70$ counts s^{-1} or which is surrounded by coincidence-loss-induced mod-8 pattern (flag bit 4) is considered a potential source of a readout streak. Sources situated within a threshold distance of the potential readout streak are flagged. The threshold distance is 8 arcsec unless the read out streak is produced by a source with a count rate > 220 counts s^{-1}, in which case the threshold distance is set to 9.5 arcsec. The source responsible for a readout streak may not be located on the image because it may fall outside the data collection window. A further test is performed in these cases. The counts in a raw image are described by the array C_{ij} where i is the column number and j is the row number. Based on data screening, our criteria for a column containing a potential readout streak is provided by the six conditions $C_{ij} > C_{(i-k)j}$ where $k = -3$, -2, -1, 1, 2, 3. If each crtierion is met individually over >60 per cent of the pixel rows then any source situated within 19 rows of the column are flagged as occurring over a potential readout streak.

B.2 Flag 2: smoke ring

Sources containing raw count rates $\geqslant$ 60 counts s^{-1} or surrounded by a coincidence-loss-induced modulo-8 pattern (flag bit 4) are considered generators of smoke-rings. A smoke ring is located approximately along a radial line from the field centre through the star which generates it. The smoke ring is displaced towards the field edge by an amount which is non-linear with off-axis angle. The location of each ring in the raw image pixels (i_{sr},j_{sr}) is predicted using the following parameterization:

$$i_{sr} = (A_1 + i_c) + A_2 x + A_3 y + A_4 x^2 + A_5 y^2 + A_6 xy \quad (1)$$

$$j_{sr} = (B_1 + j_c) + B_2 x + B_3 y + B_4 x^2 + B_5 y^2 + B_6 xy \quad (2)$$

where (ic,jc) = (1024.5,1024.5) is the center of the FOV, and $(x,y) = (i_* - i\mathrm{c}, j_* - j\mathrm{c})$. The coefficients $A_{1\ldots6}$ and

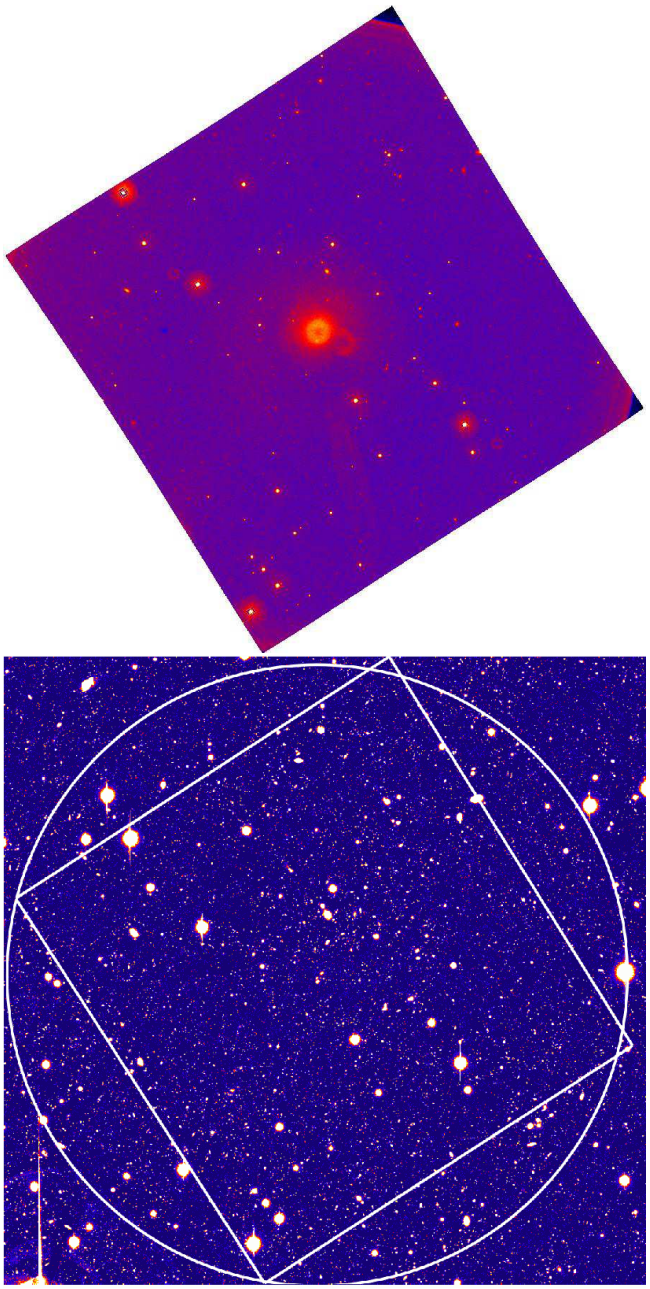

Figure A2. The 13-hour *XMM-Newton*/*Chandra* deep field. The top panel contains the XMM-OM B-filter image. The bright, circular region at the centre of the image is the central enhanced region referred to in Section 3.9.6. The bottom panel contains the corresponding Subaru B-filter image with the OM field of view (diamond) overlayed. The XMM-OM is not sensitive to sources outside of the overlayed circle, hence XMM-OM and Subaru source detection characteristics are based only on sources within the overlapping region of the circle and diamond.

$B_{1...6}$ were determined from a least squares fit to a random sample of 100 smoke rings, and are given in Table B1.

B.3 Flag 3: diffraction spike

All catalogue objects with either raw count-rates $\geqslant$ 70 counts s^{-1} or flagged as being surrounded by a coincidence-loss-induced modulo-8 pattern (flag bit 4) have been tested for diffraction spikes. We compare source number densities

Table B1. Coefficients for smoke ring locations.

n	A_n	B_n
1	9.6950	-4.8165
2	1.2052	5.0884×10^{-4}
3	1.1027×10^{-3}	1.2071
4	2.9117×10^{-6}	-2.8810×10^{-7}
5	1.8790×10^{-6}	1.5490×10^{-6}
6	4.2437×10^{-7}	-1.0783×10^{-6}

$n_{\rm box}$ and $n_{\rm spk}$where $n_{\rm box}$ is the density of objects with raw count rates < 5 counts s^{-1} within a box 70×70 arcsec^2 centred on the bright source, and $n_{\rm spk}$ is the average density of objects with raw count rates < 5 counts s^{-1} within four rectangular regions oriented radially away from the bright source in directions 45°, 135°, 225° and 315° of dimensions (10×52) arcsec^2, starting 5 arcsec from the position of the bright source. These four rectangular regions correspond to the locations of the putative diffraction spikes. If $n_{\rm spk} > 3n_{\rm box}$, all detections < 5 arcsec from the diffraction spikes are flagged. Note that this algorithm will inevitably be less effective in crowded fields.

B.4 Flag 4: bright source surrounded by coincidence-loss-induced modulo-8 pattern

If the brightest pixel within a 4 arcsec x 4 arcsec box centered on a detection has a count rate > 10 counts s^{-1} then the object is flagged as a bright source with surrounding mod-8 structure. If the brightest pixel has a count rate which is < 10 counts s^{-1}, but > 0.5 counts s^{-1} then the source undergoes a further test: a pattern search algorithm is performed on the regions $5 - 15$ arcsecond to the left, right, above and below the source in raw image coordinates. The pattern search checks for a 10-arcsec-long column to the left or right of the source, or a 10-arcsec-long row above or below the source, which has all of its pixels lower in value than all of the pixels in one of the surrounding columns or rows. If such a pattern is identified in two or more of the four sides of the source, then the source is flagged.

APPENDIX C: COLUMNS IN THE XMM-SUSS SOURCE TABLE

The XMM-SUSS fits table contains two extensions. The first extension provides the source catalogue, and the second extension lists the XMM-Newton observations from which the catalogue was constructed. The column headings for the XMM-SUSS source catalogue table are listed in Table C1, and we now provide a brief description of the columns. Filter-specfic entries are set to 'NULL' for filters in which the source is not detected. Column 1 gives the source name in International Astronomical Union format. Columns 2 and 3 refer to the *XMM-Newton* observation in which the source was found; column 2 is the corresponding row number in the second extension of the fits file (which lists the *XMM-Newton* observations) and column 3 gives the 10 digit observation identification number (OBSID) of the observation. Column 4 gives the source number within the merged source list deriving from that observation (this number is only unique to the source within the relevant *XMM-Newton* observation, not within the XMM-SUSS as a whole). Col-

umn 5 is a unique reference number for the source within the XMM-SUSS. Columns 6–11 gives the distance in arcsec of the source to the nearest celestial source in the catalogue which is detected in the named filter. Note that as the catalogue only contains sources which are detected in the UV, the nearest source in any filter must (also) have been detected in at least 1 UV band. Columns 12–15 give the right ascention and declination of the source in decimal and hexagesimal formats. Column 16 gives the 1-σ position uncertainty in arcsec. Columns 17 and 18 give the Galactic longitude and latitude in degrees. Column 19 gives the number of different *XMM-Newton* observations in which the source has been detected. Since a source is given a separate row for each *XMM-Newton* observation in which it is detected, column 19 also corresponds to the number of rows in which the source appears in the XMM-SUSS. Columns 20–25 give the number of exposures within the *XMM-Newton* observation in which the source is detected in each filter. Columns 26–31 give the detection significance of the source in each filter. Columns 32–43 give the count rates and uncertainties in each filter. Columns 44–55 give, for each filter, the flux density and uncertainty at the effective wavelength (Table 1) of the filter. Columns 56–67 give the AB magnitudes and errors, and columns 68–79 the Vega-based magnitudes and errors. Columns 80–91 give for each filter the χ^2/ν value for a constant source countrate and the maximum deviation from the median countrate in terms of σ, for sources detected multiple times through the same filter, in the same *XMM-Newton* observation (see Section 5.3). Columns 92–109 give, for each filter, the sizes of the major and minor axes of the source in arcsec and the position angle of the major axis. Columns 110–115 give the quality flags as integer numbers (derived from the sum of the flag bit values) for the different filters and columns 116–121 give the quality flags as strings of logical values corresponding to the flag bits (T and F when the flag is set or not set respectively). Columns 122–127 state whether the source appears to be pointlike (value 0) or extended (value 1) in each of the filters.

Table C1. Column names in the XMM-SUSS table.

Column number	Column name	Column number	Column name
1	IAUNAME	65	B_AB_MAG_ERR
2	N_SUMMARY	66	V_AB_MAG
3	OBSID	67	V_AB_MAG_ERR
4	SRCID	68	UVW2_VEGA_MAG
5	SRCNUM	69	UVW2_VEGA_MAG_ERR
6	UVW2_SRCDIST	70	UVM2_VEGA_MAG
7	UVM2_SRCDIST	71	UVM2_VEGA_MAG_ERR
8	UVW1_SRCDIST	72	UVW1_VEGA_MAG
9	U_SRCDIST	73	UVW1_VEGA_MAG_ERR
10	B_SRCDIST	74	U_VEGA_MAG
11	V_SRCDIST	75	U_VEGA_MAG_ERR
12	RA	76	B_VEGA_MAG
13	DEC	77	B_VEGA_MAG_ERR
14	RA_HMS	78	V_VEGA_MAG
15	DEC_DMS	79	V_VEGA_MAG_ERR
16	POSERR	80	UVW2_CHI2
17	LII	81	UVW2_MAXDEV
18	BII	82	UVM2_CHI2
19	N_OBSID	83	UVM2_MAXDEV
20	N_UVW2_EXP	84	UVW1_CHI2
21	N_UVM2_EXP	85	UVW1_MAXDEV
22	N_UVW1_EXP	86	U_CHI2
23	N_U_EXP	87	U_MAXDEV
24	N_B_EXP	88	B_CHI2
25	N_V_EXP	89	B_MAXDEV
26	UVW2_SIGNIF	90	V_CHI2
27	UVM2_SIGNIF	91	V_MAXDEV
28	UVW1_SIGNIF	92	UVW2_MAJOR_AXIS
29	U_SIGNIF	93	UVM2_MAJOR_AXIS
30	B_SIGNIF	94	UVW1_MAJOR_AXIS
31	V_SIGNIF	95	U_MAJOR_AXIS
32	UVW2_RATE	96	B_MAJOR_AXIS
33	UVW2_RATE_ERR	97	V_MAJOR_AXIS
34	UVM2_RATE	98	UVW2_MINOR_AXIS
35	UVM2_RATE_ERR	99	UVM2_MINOR_AXIS
36	UVW1_RATE	100	UVW1_MINOR_AXIS
37	UVW1_RATE_ERR	101	U_MINOR_AXIS
38	U_RATE	102	B_MINOR_AXIS
39	U_RATE_ERR	103	V_MINOR_AXIS
40	B_RATE	104	UVW2_POSANG
41	B_RATE_ERR	105	UVM2_POSANG
42	V_RATE	106	UVW1_POSANG
43	V_RATE_ERR	107	U_POSANG
44	UVW2_AB_FLUX	108	B_POSANG
45	UVW2_AB_FLUX_ERR	109	V_POSANG
46	UVM2_AB_FLUX	110	UVW2_QUALITY_FLAG
47	UVM2_AB_FLUX_ERR	111	UVM2_QUALITY_FLAG
48	UVW1_AB_FLUX	112	UVW1_QUALITY_FLAG
49	UVW1_AB_FLUX_ERR	113	U_QUALITY_FLAG
50	U_AB_FLUX	114	B_QUALITY_FLAG
51	U_AB_FLUX_ERR	115	V_QUALITY_FLAG
52	B_AB_FLUX	116	UVW2_QUALITY_FLAG_ST
53	B_AB_FLUX_ERR	117	UVM2_QUALITY_FLAG_ST
54	V_AB_FLUX	118	UVW1_QUALITY_FLAG_ST
55	V_AB_FLUX_ERR	119	U_QUALITY_FLAG_ST
56	UVW2_AB_MAG	120	B_QUALITY_FLAG_ST
57	UVW2_AB_MAG_ERR	121	V_QUALITY_FLAG_ST
58	UVM2_AB_MAG	122	UVW2_EXTENDED_FLAG
59	UVM2_AB_MAG_ERR	123	UVM2_EXTENDED_FLAG
60	UVW1_AB_MAG	124	UVW1_EXTENDED_FLAG
61	UVW1_AB_MAG_ERR	125	U_EXTENDED_FLAG
62	U_AB_MAG	126	B_EXTENDED_FLAG
63	U_AB_MAG_ERR	127	V_EXTENDED_FLAG
64	B_AB_MAG		